ARTICLES

Peristaltically driven channel flows with applications toward micromixing[a]

Kiril P. Selverov[b] and H. A. Stone[c]
Division of Engineering and Applied Sciences, Harvard University, Cambridge, Massachusetts 02138

Flows driven by a transverse, small amplitude traveling wave propagating along the boundary of a closed rectangular container are examined. High-frequency motions are the primary focus of interest, although low-frequency results are discussed also. Using asymptotic analysis appropriate for high frequencies, the steady, time-independent (streaming) flow is computed analytically and compared with results of the exact calculation. The boundary-layer structure is delineated and average Eulerian and Lagrangian flow characteristics are compared. Experiments confirming the major qualitative high-frequency findings are reported in an Appendix. The results could be useful for modeling peristaltically operated microelectromechanical systems devices where fluid motion needs to be produced without internal moving mechanical components. © *2001 American Institute of Physics.* [DOI: 10.1063/1.1377616]

I. INTRODUCTION

The rapid advances in making microelectromechanical systems (MEMS) have produced a variety of devices and new applications that involve basic mechanical and fluid dynamical design considerations.[1] Viscous effects are typically very important on the small $(1–100\ \mu m)$ scales being considered and there is a need to produce fluid motion in MEMS without utilizing the familiar mechanical elements present in common pumps and valves. In particular, fluid motions driven by small amplitude displacements of a boundary have been demonstrated.[2,3] Alternative methods for (laminar flow) mixing and transport at the microscale are being developed also.[4] Motivated by these experimental demonstrations and possible applications to mixing in small geometries, we have examined flows driven by transversely oscillating boundaries in a closed two-dimensional rectangular geometry. The ability to generate directed transport (i.e., a mean flow) over time was investigated, and the influence of inertial effects was examined. Particular attention was given to the high-frequency limit that is representative of the prototype MEMS devices.

The confined fluid motions that we have examined are driven by a peristaltic wave—a progressive wave of area expansion or contraction propagating along the length of a flexible boundary.[5] A preliminary version of our study was presented in the *ASME Mechanical Congress and Exposition* in 1998.[6] In published experiments, the wall motion was produced with the help of arrays of alternating piezoelectric el-

ements placed along the surface.[2,3] Typically, the driving wave is of small amplitude compared to the channel height, a case that is relevant to MEMS because large amplitudes bring the boundaries close together and might cause them to stick to each other, which can permanently disable a device. In the devices constructed to date, typical amplitudes are 10^{-6} cm, channel dimensions are $h \approx 10^{-2}$ cm, and driving frequencies ω range between $10^3–10^6$ Hz.[2,3] For water, $\nu = O(10^{-2})$ cm^2/s, and therefore the dimensionless frequency $\alpha^2 = \omega h^2/\nu \gg 1$, which is an important parameter in the analysis reported below. We will thus be most interested in the high-frequency case. Since one application of this mechanism for generating fluid motion is to small scale transport and mixing, we will assume that the channel is closed at both ends.

Similar fluid dynamical studies have been performed previously in an attempt to understand the details of fluid motions involved in peristaltic pumping, owing to applications to transport processes in biological fluid dynamics and acoustic streaming. For peristaltically driven motions, limiting cases that have been studied analytically and numerically include long wavelength motions,[5,7,8] zero-,[5,9,10] small-,[8] or finite-Reynolds-number flows,[7,11,12] and small[7,9–12] or finite[5,8] oscillation amplitudes (see the next section for definitions). Our work has elements in common with these studies, but in addition to including inertial effects throughout, we focus on the high-frequency limit and, in general, are able to obtain analytical expressions using asymptotic analysis. The spirit of the analysis also has features similar to studies of acoustic streaming (e.g., Riley;[13] see also Riley[14] and Nyborg[15]), which normally refers to time-independent motions produced by the oscillatory component of a bulk flow; in our case the oscillations derive from the transverse

[b] Electronic mail: kiril@stokes.deas.harvard.edu
[c] Telephone: (617)495-3599; fax: (617)495-9837. Electronic mail: has@stokes.deas.harvard.edu

motion of the boundary. Finally, our analysis of the boundary-layer near the fixed boundary shares elements in common with studies of wave-driven mass transport near the sea bottom and sea surface (e.g., Longuet-Higgins[16] and Mei[17]). These studies consider a known potential flow field, and examine the net Lagrangian transport near the boundaries. Our results are consistent with these studies in that transport near a fixed boundary is in the direction of the driving wave, which is the case for high frequencies ($\alpha \gg 1$). We also provide a detailed description of the boundary-layer structure and the velocity field both near and far from the boundaries for the case of the dimensionless frequency $\alpha \gg 1$ (which is relevant to MEMS), and explicitly indicate the dependence of all quantities on α; viscous flow near the oscillating boundary constitutes the dominant flow when $\alpha \gg 1$. Thus, our investigation provides a link between studies of peristaltic pumping, acoustic streaming, and wave-driven motions.

In the biofluids literature, peristaltically driven motions have been examined many times. One of the important transport questions concerns ''reflux,'' which refers to net fluid motion opposite to the direction of the traveling wave. Fung and Yih,[11] motivated by questions of fluid transport within the ureter, found that peristaltic pumping against an adverse pressure gradient may result in a negative net *Eulerian* velocity near the center of the channel. Weinberg, Eckstein and Shapiro[18] and Jaffrin and Shapiro[19] later argued that reflux should be defined not in the *Eulerian*, but rather in the *Lagrangian* sense as a net displacement of a material particle in the direction opposite to the traveling wave. In particular, for peristaltic flows, Shapiro and Jaffrin[20] showed that net Eulerian and Lagrangian velocities can differ significantly. They studied low-Reynolds-number flows ($\alpha < 1$) and concluded for a certain range of parameters that reflux should occur near the channel walls rather near the center. Yin and Fung[12] also employed the Lagrangian view of reflux and showed experimentally for low-Reynolds-number flows that material particles near the oscillating wall travel in the direction opposite to the wave. Subsequently, Takabatake, Ayukawa and Mori[21] used a numerical study of two-dimensional peristaltic transport to show that reflux defined in the Lagrangian sense occurs near the channel walls for low-Reynolds-number flows. For high-Reynolds-number flows, however, net Lagrangian transport near the channel walls is in the direction of the traveling wave and reflux occurs near the channel center.

Our asymptotic study of peristaltic pumping agrees with all of the results above, providing in addition an analytical description of the resulting net flow with clearly indicated dependence on the pumping frequency. When characterizing reflux, a Lagrangian description is necessary as has been the more generally adopted view in recent literature. We show that at high pumping frequencies, $\alpha \gg 1$ (corresponding to high-Reynolds-number flows in the studies mentioned above), which are the main focus of this paper, net Lagrangian transport near the channel wall is in the direction of the traveling wave, with reflux occurring near the channel center in the case of a channel closed at both ends. At low pumping frequencies, $\alpha \ll 1$, or low-Reynolds-number flows, both re-
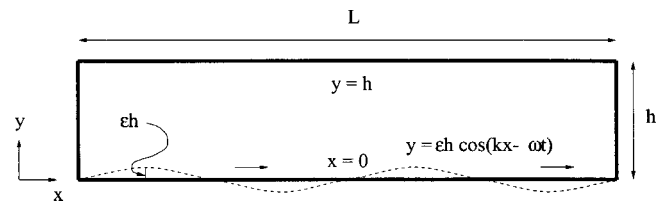

FIG. 1. One of the walls of a long ($L/h \gg 1$) rectangular channel undergoes a sinusoidal oscillation in the form of a traveling wave. In the analysis reported here the channel is assumed to be closed at both ends.

flux behaviors may be observed for a channel closed at both ends: net Lagrangian transport near the channel wall may be opposite to the wave at certain positions along the channel, indicating that reflux occurs near the oscillating wall, while at other positions along the channel reflux could be occurring near the channel center. The former behavior is observed for most positions x along the channel; thus, for low-frequency flows, reflux is mostly near the channel walls. Only at very few positions along the channel, due to a standing wave established by the presence of rigid side walls in our problem, reflux occurs near the channel center, causing the flow to have a cellular structure with cells of width one wavelength of the driving wave. When our work was near completion, we learned of a related recent study by Yi, Bau, and Hu.[22] These authors primarily present a numerical investigation valid for arbitrary surface amplitudes, and investigate some aspects of mixing patterns.

We begin with a dimensionless problem statement in Sec. II. The leading-order, high-frequency analytical solution is given in Sec. III and the time-averaged streaming flow is determined in Sec. IV. The main features of the flow are summarized in Sec. V and a comparison of the time-averaged Eulerian and Lagrangian flow characteristics is given in Sec. VI. Some remarks about mixing effectiveness of these flows are given in the conclusions. The appendices provide intermediate details of some of the calculations. Also, experiments that confirm, at least qualitatively, the analytical results are reported in Appendix C.

II. PROBLEM STATEMENT

We consider the incompressible flow of a Newtonian fluid with density ρ and viscosity μ in a rectangular channel of length L and height h (see Fig. 1). The two-dimensional flow is driven by transverse oscillations of one ($y=0$) boundary in the form of a traveling, or peristaltic, wave of amplitude ϵh ($\epsilon < 1$). In particular, material points on this boundary are assumed to move according to

$$y = \epsilon h \cos(kx - \omega t). \tag{1}$$

The governing equations are the Navier–Stokes and continuity equations,

$$\rho \left(\frac{\partial \mathbf{u}}{\partial t} + \mathbf{u} \cdot \nabla \mathbf{u} \right) = -\nabla p + \mu \nabla^2 \mathbf{u} \quad \text{and} \quad \nabla \cdot \mathbf{u} = 0, \tag{2}$$

where $\mathbf{u} = u\mathbf{e}_x + v\mathbf{e}_y$, subject to the boundary conditions,

$$\mathbf{u}(x, y = \epsilon h \cos(kx - \omega t), t) = (0, \epsilon \omega h \sin(kx - \omega t)), \tag{3a}$$

$$\mathbf{u}(x, y=h, t) = \mathbf{0}. \tag{3b}$$

If a progressive wave is imposed simultaneously on the upper boundary as well, it is straightforward to modify the analysis below.

We scale lengths by h, velocities by $\epsilon\omega h$, time by ω^{-1}, pressure by $\epsilon\mu\omega$, and define the dimensionless parameters

$$\kappa = kh \quad \text{and} \quad \alpha^2 = \frac{\rho\omega h^2}{\mu} \tag{4}$$

representing, respectively, the dimensionless wave number and frequency. It is common to refer to α^2 as the Womersley number. Equations (2) and (3) can then be rewritten in dimensionless form (using the same variables as above) as

$$\alpha^2 \frac{\partial \mathbf{u}}{\partial t} + \epsilon\alpha^2 \mathbf{u} \cdot \nabla \mathbf{u} = -\nabla p + \nabla^2 \mathbf{u} \quad \text{and} \quad \nabla \cdot \mathbf{u} = 0 \tag{5}$$

subject to

$$\mathbf{u}(x, \epsilon\cos(\kappa x - t), t) = (0, \sin(\kappa x - t)), \tag{6a}$$

$$\mathbf{u}(x, 1, t) = \mathbf{0}. \tag{6b}$$

Since ϵ represents the dimensionless amplitude of the driving wave, small amplitudes have $\epsilon \ll 1$.

We note that other authors have chosen nondimensional parameters somewhat differently. In particular, it is common to utilize ϵ, κ, and $\mathcal{R} = hc/\nu = h\omega/\nu k$, where $\nu = \mu/\rho$ and $\mathcal{R}$ is a Reynolds number based on the wave speed $c = \omega/k$. Here $\mathcal{R}\kappa = \alpha^2$.

We wish to indicate also that alternative formulations of such traveling wave problems are possible and have been employed previously by some authors. In particular, Eqs. (5) above could be written in the reference frame of the traveling wave. We have found it convenient to account for the time-dependence in a different, but related, fashion, as described in Sec. III.

If the channel is closed, an additional integral constraint over a cross section of the channel must be imposed,

$$\int_{\epsilon\cos(\kappa x - t)}^{1} u(x, y, t)\, dy = -\frac{\cos(\kappa x - t) - \cos(t)}{\kappa}. \tag{7}$$

Constraint (7) is obtained by integrating the continuity equation across the channel and using the fact that the horizontal velocity $u(x, y, t)$ is zero on all walls, including the side walls at $x = \pm L/2$. We thank Yi, Bau, and Hu[22] for indicating the necessity of this integral constraint which had been overlooked in the initial draft reporting our results. The x-independent part of this constraint necessitates the existence of an x-independent leading-order solution, which in turn causes the time-averaged net flow in the channel to have x-periodic structure. We also note, that if a different boundary condition is applied at the side walls $x = \pm L/2$, the x-independent part of this integral constraint can differ substantially. In particular, if the side walls are allowed to be flexible with certain prescribed motion, it is possible that this x-independent part is identically zero, causing the x-periodic component of the time-averaged velocity field computed in this paper to be identically zero as well. An absence of the x-independent part of this constraint can also be due to an absence of rigid side walls, but a presence of an adverse pressure gradient allowing fluid to freely move both horizontally and vertically at $x = \pm L/2$, but working against the pumping so as to cause a zero net flux across a vertical cross section of the channel. As we present our findings, we will comment on the distinction between the "underlying" flow independent of the existence of side walls, and the additional standing wave flow set up by such walls.

There are many papers in the peristaltic flows literature that study analytically the low-Reynolds-number ($\alpha \ll 1$), long-wave ($\kappa \ll 1$) limits, but only a few that consider the role of inertia, and there is no work to our knowledge that has established analytical results for the high-frequency, $\alpha \gg 1$, limit (of most interest to MEMS) in a closed domain. We provide such results below. These results may be especially useful since numerical calculations for this kind of problems often have computational difficulties when α is large.[22]

III. ANALYTICAL SOLUTION FOR HIGH FREQUENCIES AND $\epsilon \ll 1$

Consider Eqs. (5)–(6) in the limit $\epsilon \ll 1, \kappa = O(1)$ and $\alpha \gg 1$. Also, consider the channel to be long compared to both the channel width and the wavelength of the driving wave, $L/h \gg 1$, $L \gg 2\pi/k$, so that the direct effect of the side walls $x = \pm L/2$ can be neglected. We seek the steady, time-independent mean flow generated as a result of the oscillation of the boundary, though if we are interested in following particle trajectories, it is necessary to know the detailed time-dependent motion. We use the perturbation expansions

$$\mathbf{u} = \mathbf{u}_0 + \epsilon\mathbf{u}_1 + \epsilon^2\mathbf{u}_2 + O(\epsilon^3)$$

and

$$p = p_0 + \epsilon p_1 + \epsilon^2 p_2 + O(\epsilon^3), \tag{8}$$

where $\mathbf{u}_i(x, y, t)$ and $p_i(x, y, t)$ are $O(1)$ and independent of ϵ, but depend on κ and α. Also, via a Taylor series, we expand the velocity at the moving wall around the equilibrium position $y = 0$,

$$\mathbf{u}(x, y = \epsilon\cos(\kappa x - t), t) = \mathbf{u}(x, 0, t) + \epsilon\cos(\kappa x - t)$$

$$\times \frac{\partial \mathbf{u}}{\partial y}(x, 0, t) + O(\epsilon^2). \tag{9}$$

For $\alpha \gg 1$, which is the main focus of this paper, there are boundary layers of thickness $O(\alpha^{-1})$, so in addition to $\epsilon \ll 1$, expansion (9) requires that $\epsilon\alpha \ll 1$, i.e., $\epsilon \ll \alpha^{-1} \ll 1$. In a similar manner we expand the integral constraint (7),

$$\int_0^1 u(x, y, t)\, dy - \epsilon u(x, 0, t)\cos(\kappa x - t) + O(\epsilon^2)$$

$$= -\frac{\cos(\kappa x - t) - \cos(t)}{\kappa}. \tag{10}$$

A. The structure of the leading-order solution

The dominant flow $\mathbf{u}_0$ satisfies the unsteady Stokes equations and boundary conditions

$$\nabla^2 \mathbf{u}_0 - \nabla p_0 = \alpha^2 \frac{\partial \mathbf{u}_0}{\partial t}, \quad \nabla \cdot \mathbf{u}_0 = 0, \tag{11a}$$

$$\mathbf{u}_0(x,0,t) = (0, \sin(\kappa x - t)), \quad \mathbf{u}_0(x,1,t) = \mathbf{0}, \tag{11b}$$

with the integral constraint

$$\int_0^1 u_0 \, dy = -\frac{\cos(\kappa x - t)}{\kappa} + \frac{\cos(t)}{\kappa}. \tag{12}$$

This problem is similar to Stokes' second problem and the Womersley problem (pipe flow driven by a periodic pressure gradient, e.g., Leal[23]). We note that Eqs. (11) and (12) imply a leading-order velocity $\mathbf{u}_0$ consisting of two linearly independent parts—a part periodic in $\kappa x - t$ and a part periodic in t and independent of x. Both parts have zero average in time. It is straightforward to solve (11) analytically, both for an arbitrary α and asymptotically for $\alpha \gg 1$, and we have completed both calculations. The detailed solution for an arbitrary α is given in Appendix A and was originally presented by Fung and Yih.[11] While the solution for arbitrary α is more general, it does not clearly show the dependence of the velocity on α—indeed, this dependence is complicated. Thus, for $\alpha \gg 1$, it is advantageous to construct an asymptotic solution which will be useful for determining the analytical structure of the $O(\epsilon)$ correction to the flow. The method of matched asymptotic expansions is used (e.g., Ref. 24), and since the overall expansion involves two small parameters, ϵ and α^{-1}, as well as "inner" and "outer" representations, the notation is somewhat complicated. We have tried to simplify it as much as possible in order to maintain focus on the physical results of interest.

For a closed channel the pressure gradient has to scale as the dominant term in Eq. (11). Thus, we rescale the pressure as

$$p_0' = p_0 / \alpha^2. \tag{13}$$

For $\alpha \gg 1$ we then consider

$$\alpha^{-2} \nabla^2 \mathbf{u}_0 = \frac{\partial \mathbf{u}_0}{\partial t} + \nabla p_0', \quad \nabla \cdot \mathbf{u}_0 = 0, \tag{14}$$

and so we expect that the dominant flow $\mathbf{u}_0 = (u_0, v_0)$ has a boundary-layer structure. Throughout most of the channel, away from the walls, we can neglect the terms $O(\alpha^{-2})$ and seek a solution obeying the inviscid equations

$$\frac{\partial u_0^o}{\partial x} + \frac{\partial v_0^o}{\partial y} = 0, \tag{15a}$$

$$\frac{\partial u_0^o}{\partial t} + \frac{\partial p_0'^o}{\partial x} = 0, \tag{15b}$$

$$\frac{\partial v_0^o}{\partial t} + \frac{\partial p_0'^o}{\partial y} = 0, \tag{15c}$$

where a superscript "o" indicates that this is the "outer" solution to a boundary-layer problem, subject to

$$v_0^o(x,0,t) = \sin(\kappa x - t), \quad v_0^o(x,1,t) = 0. \tag{16}$$

We impose conditions only on the normal component of velocity since Eqs. (15) are first order.

Near the walls, within boundary layers of thickness $O(\alpha^{-1})$, velocity gradients are large and the neglected $O(\alpha^{-2})$ viscous term in (14) becomes important. To consider these boundary layers we rescale the y variable as

$$y' = \alpha y, \quad y^* = 1 - \alpha(1 - y), \tag{17}$$

for the boundary layers near $y = 0$ and $y = 1$, respectively. We thus obtain the boundary-layer equations,

$$\alpha^{-1} \frac{\partial u_0^i}{\partial x} + \frac{\partial v_0^i}{\partial y'} = 0, \tag{18a}$$

$$\frac{\partial^2 u_0^i}{\partial y'^2} - \frac{\partial p_0'^i}{\partial x} = \frac{\partial u_0^i}{\partial t}, \tag{18b}$$

$$\alpha^{-1} \frac{\partial^2 v_0^i}{\partial y'^2} - \frac{\partial p_0'^i}{\partial y'} = \alpha^{-1} \frac{\partial v_0^i}{\partial t}, \tag{18c}$$

where y' is replaced by y^* when discussing the boundary layer near $y = 1$, a superscript "i" denotes that this is the "inner" solution to a boundary-layer problem, and terms $O(\alpha^{-2})$ and smaller are neglected.

Equations (18) suggest a solution of the form

$$\mathbf{u}_0 = \mathbf{u}_{00} + \alpha^{-1} \mathbf{u}_{01} + \text{h.o.t.}, \quad p_0' = p_{00}' + \alpha^{-1} p_{01}' + \text{h.o.t.}, \tag{19}$$

where $\mathbf{u}_{0i}(x,y,t)$ and $p_{0i}'(x,y,t)$ are independent of α. The next two sections describe the solution to the outer and inner problems stated above, both at leading order and $O(\alpha^{-1})$. These solutions are then used to compute the time-averaged flow $\langle \mathbf{u}_1 \rangle$.

B. The leading-order velocity u₀₀

The leading-order outer velocity $\mathbf{u}_{00}^o$ is the solution to the system (15) subject to (16). These equations are solved to obtain

$$u_{00}^o(x,y,t) = -\frac{\cos(\kappa x - t)\cosh(\kappa(1-y))}{\sinh(\kappa)} + \frac{\cos(t)}{\kappa}, \tag{20a}$$

$$v_{00}^o(x,y,t) = \frac{\sin(\kappa x - t)\sinh(\kappa(1-y))}{\sinh(\kappa)}, \tag{20b}$$

$$p_{00}'^o(x,y,t) = P_0(t) - \frac{\cos(\kappa x - t)\cosh(\kappa(1-y))}{\kappa \sinh(\kappa)} + \frac{\sin(t)}{\kappa} x, \tag{20c}$$

where $P_0(t)$ is a reference pressure. Plots of this solution are given in Fig. 2. We note that the x-component of velocity is in general nonzero at $y = 0$, which violates no-slip and presupposes the existence of boundary layers (i.e., the inner solutions). We also note that the x-independent part of the horizontal velocity, $U_{00}^o = \cos(t)/\kappa$, is due to the presence of rigid side walls in the channel; if an adverse pressure gradient causing zero net flux across a cross section of the channel is imposed instead, this part would be identically zero.

The boundary-layer equations that the leading-order inner velocity $\mathbf{u}_{00}^i$ satisfies are
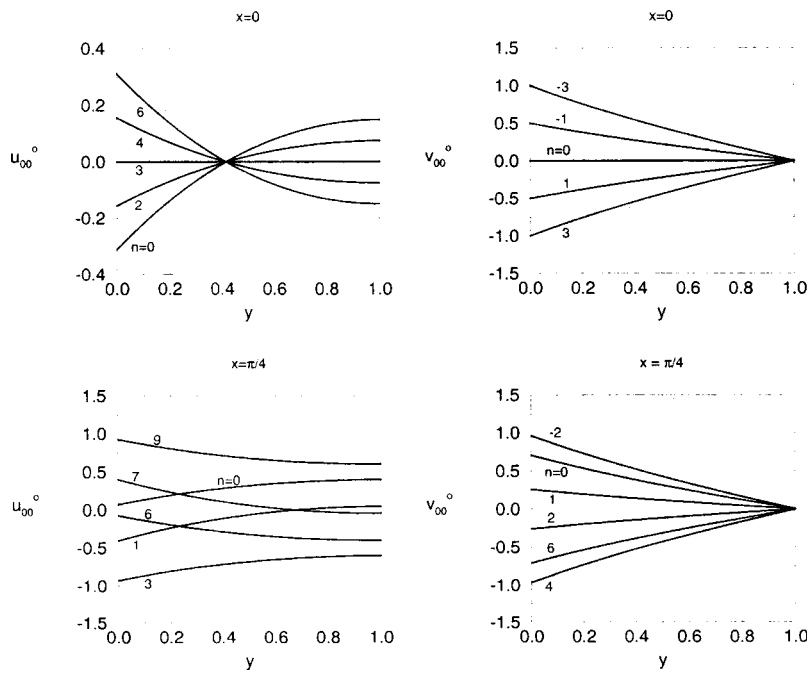
FIG. 2. Velocity profiles according to Eqs. (20) of the time-dependent, traveling-wave-driven, leading-order outer flow $\mathbf{u}_{00}^o$ in a long, closed channel, at fixed $x=0$ and $x=\pi/4$, away from the walls; $t=n\pi/6$; $\kappa=1$. u_{00}^o denotes the component along the channel, v_{00}^o denotes the component across the channel, and y denotes the coordinate across the channel.

$$\frac{\partial v_{00}^i}{\partial y'}=0, \tag{21a}$$

$$\frac{\partial^2 u_{00}^i}{\partial y'^2}-\frac{\partial p_{00}'^i}{\partial x}=\frac{\partial u_{00}^i}{\partial t}, \tag{21b}$$

$$\frac{\partial p_{00}'^i}{\partial y'}=0, \tag{21c}$$

which are obtained from (18) by neglecting terms $O(\alpha^{-1})$ and smaller. The boundary conditions are determined by matching the inner with the corresponding outer solutions given by (20) (e.g., Ref. 24). In the boundary layer near $y=0$ we thus require that

$$u_{00}^{i0}(x,y'=0,t)=0, \tag{22a}$$

$$\lim_{y'\to\infty} u_{00}^{i0}=\lim_{y\to 0}u_{00}^{o}=-\cos(\kappa x-t)\coth(\kappa)+\cos(t)/\kappa, \tag{22b}$$

$$v_{00}^{i0}(x,y'=0,t)=\sin(\kappa x-t),\ \lim_{y'\to\infty} v_{00}^{i0}=\lim_{y\to 0}v_{00}^{o}=\sin(\kappa x-t), \tag{22c}$$

where a superscript $i0$ denotes the solution to the inner problem in the boundary layer near $y=0$. Equations (21) subject to (22) have the solution

$$u_{00}^{i0}(x,y',t)=\mathrm{Re}\left\{\left(e^{\iota(\kappa x-t)}\coth(\kappa)-\frac{e^{-\iota t}}{\kappa}\right)\right.$$
$$\left.\times(e^{(\sqrt{2}/2)(\iota-1)y'}-1)\right\}$$
$$=\coth(\kappa)\left(e^{-(\sqrt{2}/2)y'}\cos\left(\kappa x-t+\frac{\sqrt{2}}{2}y'\right)\right.$$
$$-\cos(\kappa x-t)\bigg)$$
$$-\frac{1}{\kappa}\left(e^{-(\sqrt{2}/2)y'}\cos\left(\frac{\sqrt{2}}{2}y'-t\right)-\cos(t)\right), \tag{23a}$$

$$v_{00}^{i0}(x,y',t)=\sin(\kappa x-t), \tag{23b}$$

$$p_{00}'^{i0}(x,y',t)=P_0(t)-\kappa^{-1}\cos(\kappa x-t)\coth(\kappa)+\frac{\sin(t)}{\kappa}x. \tag{23c}$$

We have given the expression for u_{00}^{i0} also in terms of $\mathrm{Re}\{[e^{\iota(\kappa x-t)}-e^{\iota t}](\cdots)\}$ since this form emphasizes that the time-average of this solution is zero.

In a similar manner, the flow in the boundary layer near $y=1$ must satisfy the boundary conditions

$$u_{00}^{i1}(x,y*=1,t)=0, \tag{24a}$$

$$\lim_{y*\to-\infty} u_{00}^{i1}=\lim_{y\to 1}u_{00}^{o}=-\cos(\kappa x-t)\mathrm{csch}(\kappa)+\cos(t)/\kappa, \tag{24b}$$

$$v_{00}^{i1}(x,y*=1,t)=0,\ \lim_{y*\to-\infty} v_{00}^{i1}=\lim_{y\to 1}v_{00}^{o}=0, \tag{24c}$$
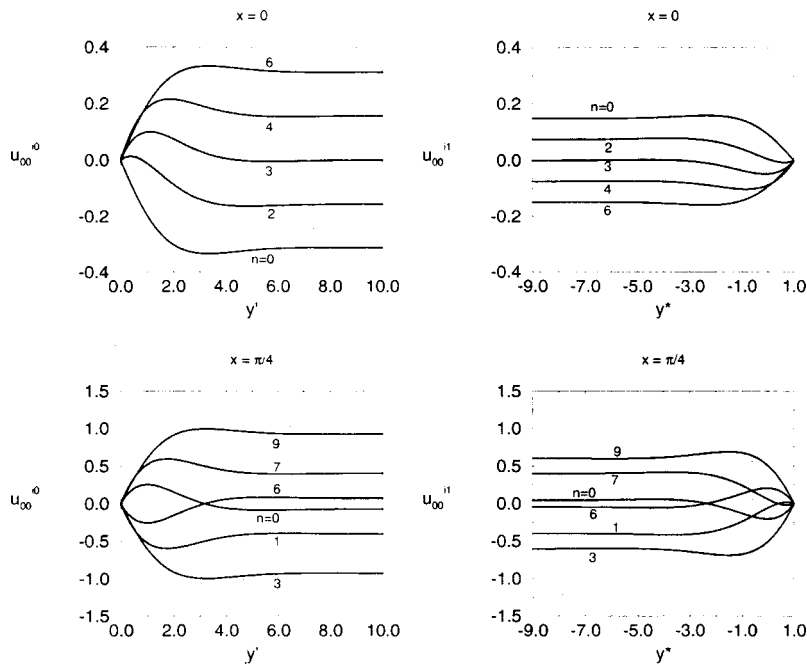
FIG. 3. Velocity profiles [Eqs. (23a) and (25a)] of the time-dependent, traveling-wave-driven, leading-order inner flow u_{00}^i in a long closed channel, in the boundary layers near the walls, at a fixed $x=0$ and $x=\pi/4$; $t=n\pi/6$ and $\kappa=1$. u_{00}^i denotes the component along the channel and y' and y^* denote the boundary-layer coordinates across the channel.

where the superscript $i1$ stands for the inner solution near $y=1$. Solutions to (21) subject to (24) are given by

$$u_{00}^{i1}(x,y^*,t)=\mathrm{Re}\left\{\left(e^{\iota(\kappa x-t)}\mathrm{csch}(\kappa)-\frac{e^{-\iota t}}{\kappa}\right)\right.$$

$$\left.\times(e^{(\sqrt{2}/2)(\iota-1)(1-y^*)}-1)\right\}$$

$$=\mathrm{csch}(\kappa)\left(e^{-(\sqrt{2}/2)(1-y^*)}\right.$$

$$\times\cos\left(\kappa x-t+\frac{\sqrt{2}}{2}(1-y^*)\right)$$

$$\left.-\cos(\kappa x-t)\right)-\frac{1}{\kappa}\left(e^{-(\sqrt{2}/2)(1-y^*)}\right.$$

$$\left.\times\cos\left(\frac{\sqrt{2}}{2}(1-y^*)-t\right)-\cos(t)\right), \tag{25a}$$

$$v_{00}^{i1}(x,y^*,t)=0, \tag{25b}$$

$$p_{00}'^{i1}(x,y^*,t)=P_0(t)-\kappa^{-1}\cos(\kappa x-t)\mathrm{csch}(\kappa)+\frac{\sin(t)}{\kappa}x. \tag{25c}$$

As with the outer solution, the presence of x-independent components in the horizontal velocities is due to the rigid side walls in the channel. Plots of the leading-order boundary-layer velocities along the channel, u_{00}^i, are shown in Fig. 3 for each boundary layer. The boundary-layer velocities perpendicular to the channel, v_{00}^i, do not vary across the boundary layers, i.e., they are independent of y' or y^* at leading-order in α^{-1}, as required by (21a). The velocity fields computed above are similar to the ones for the well-studied Womersley problem of oscillatory, pressure-driven pipe flow, (e.g., Ref. 23), though here they are obtained by oscillating a boundary transverse to the usual flow direction.

The outer and inner solutions obtained above can be used to construct leading-order velocity and pressure profiles valid uniformly across the channel by adding the outer and inner expansions and subtracting the overlap parts (see Ref. 24)

$$\mathbf{u}_{00}=\mathbf{u}_{00}^o(x,y,t)+\mathbf{u}_{00}^{i0}(x,\alpha y,t)+\mathbf{u}_{00}^{i1}(x,1-\alpha(1-y),t)$$

$$-\mathbf{u}_{00}^o|_{y=0}-\mathbf{u}_{00}^o|_{y=1}, \tag{26a}$$

$$p_{00}=p_{00}^o(x,y,t)+p_{00}^{i0}(x,\alpha y,t)+p_{00}^{i1}(x,1-\alpha(1-y),t)$$

$$-p_{00}^o|_{y=0}-p_{00}^o|_{y=1}. \tag{26b}$$

The composite solution has a particularly simple form,

$$u_{00}(x,y,t)=\mathrm{Re}\left\{\frac{e^{\iota(\kappa x-t)}A(y)}{\sinh(\kappa)}+\frac{e^{-\iota t}B(y)}{\kappa}\right\}, \tag{27a}$$

$$v_{00}(x,y,t)=\frac{\sin(\kappa x-t)\sinh(\kappa(1-y))}{\sinh(\kappa)}=v_{00}^o, \tag{27b}$$

$$p_{00}'(x,y,t)=P_0(t)-\frac{\cos(\kappa x-t)\cosh(\kappa(1-y))}{\kappa\,\sinh(\kappa)}$$

$$+\frac{\sin(t)}{\kappa}x=p_0^o, \tag{27c}$$

where

$$A(y)=\cosh(\kappa)e^{\alpha(\sqrt{2}/2)(\iota-1)y}+e^{\alpha(\sqrt{2}/2)(\iota-1)(1-y)}$$

$$-\cosh(\kappa(1-y)),$$

$$B(y)=1-e^{\alpha(\sqrt{2}/2)(\iota-1)y}-e^{\alpha(\sqrt{2}/2)(\iota-1)(1-y)}. \tag{28}$$

The existence of the x-independent component of $\mathbf{u}_{00}$ is due to the presence of rigid side walls in the channel. It is evident
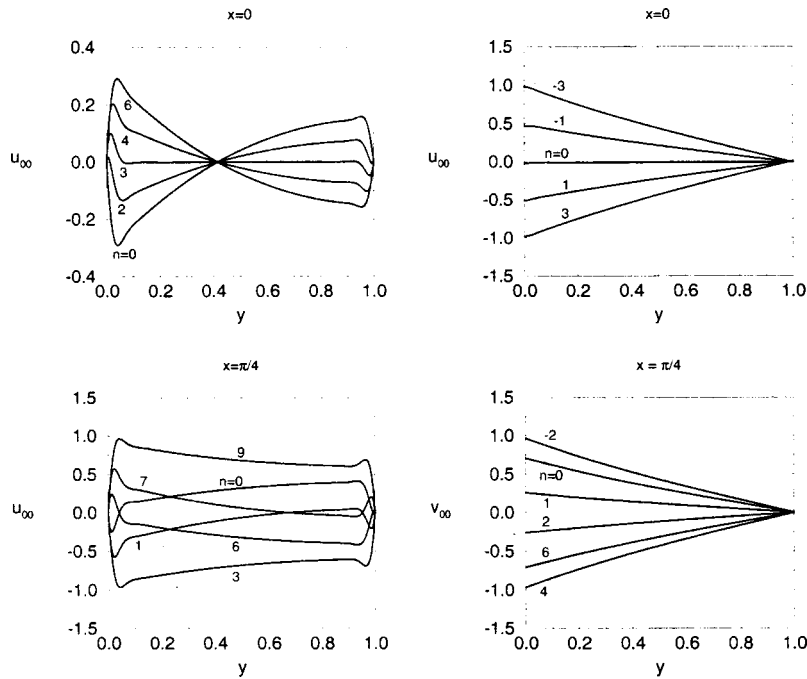
FIG. 4. Velocity profiles [Eqs. (27) and (28)] of the leading-order, uniformly valid flow $\mathbf{u}_{00}$ in a long closed channel, at a fixed x, $t = n\pi/6$ and $\kappa = 1$. u_{00} denotes the component along the channel, v_{00} denotes the component across the channel, and y denotes the coordinate across the channel; $\alpha = 70$. Note that the plot is only for half a period of the oscillation. Representative curves from the other half behave in a symmetric way and are omitted for clarity.

from (27), and expected, that $\mathbf{u}_{00}$ and p_{00} are periodic in t, with zero average in time. The leading-order flow $\mathbf{u}_{00}$ is $O(1)$ in dimensionless units everywhere in the channel. Typical velocity profiles are shown in Fig. 4 (for $\alpha = 70$ and $\kappa = 1$) and illustrate the boundary-layer structure of the dominant flows.

C. The analytical correction to $O(\alpha^{-1})$ to the leading-order velocity

Ultimately, we are interested in finding a nonzero net flow. We will show that this requires the computation of the first-order (in ϵ) velocity $\mathbf{u}_1$ which in turn relies on the knowledge of $\mathbf{u}_0$. While $\mathbf{u}_0$ is dominated by the leading-order (in α^{-1}) contribution $\mathbf{u}_{00}$ computed above, we find that to compute $\mathbf{u}_1$ with consistent accuracy and not neglect significant contributions, we must also take into account the $O(\alpha^{-1})$ correction $\mathbf{u}_{01}$ to the leading-order velocity $\mathbf{u}_{00}$. The computation of this correction follows.

The $O(\alpha^{-1})$ correction $\mathbf{u}_{01}$ [i.e., Eqs. (14) and (19)] to the velocity $\mathbf{u}_0$ is subject to the integral constraint [see (7)],

$$\int_0^1 u_{01}\,\mathrm{d}y = \frac{\sqrt{2}}{2}\frac{\sin(\kappa x - t) - \cos(\kappa x - t)}{\sinh(\kappa)}(\cosh(\kappa)+1)$$
$$+ \frac{\sqrt{2}}{\kappa}(\sin(t) + \cos(t)), \tag{29}$$

which, again, suggests a solution consisting of two linearly independent parts—a part periodic in $(\kappa x - t)$, and a part periodic in t and independent of x. Away from the walls, $\mathbf{u}_{01}$ obeys the same equations as the leading-order solution,

$$\frac{\partial u_{01}^o}{\partial x} + \frac{\partial v_{01}^o}{\partial y} = 0, \tag{30a}$$

$$\frac{\partial u_{01}^o}{\partial t} + \frac{\partial p_{01}^{\prime o}}{\partial x} = 0, \tag{30b}$$

$$\frac{\partial v_{01}^o}{\partial t} + \frac{\partial p_{01}^{\prime o}}{\partial y} = 0, \tag{30c}$$

where again a superscript o serves as a reminder that this is the outer solution to a boundary-layer problem. The boundary conditions to $\mathbf{u}_{01}^o$ cannot be stated a priori and need to be determined by matching the outer and inner representations. In the boundary layers near the walls, the correction $\mathbf{u}_{01}$ obeys the equations

$$\frac{\partial u_{00}^i}{\partial x} + \frac{\partial v_{01}^i}{\partial y'} = 0, \tag{31a}$$

$$\frac{\partial^2 u_{01}^i}{\partial y'^2} - \frac{\partial p_{01}^{\prime i}}{\partial x} = \frac{\partial u_{01}^i}{\partial t}, \tag{31b}$$

$$\frac{\partial^2 v_{00}^i}{\partial y'^2} - \frac{\partial p_{01}^{\prime i}}{\partial y'} = \frac{\partial v_{00}^i}{\partial t}, \tag{31c}$$

where a superscript i indicates that these are the inner solutions to a boundary-layer problem. Note the coupling in (31a) and (31c) of the leading-order flow $\mathbf{u}_{00}$ and the α^{-1} correction $\mathbf{u}_{01}$.

In particular, since u_{00}^i and v_{00}^i are known near each boundary [Eqs. (23a), (23b), (25a), and (25b)], Eqs. (31) can be solved analytically. We are only allowed to impose boundary conditions on the boundary-layer solutions at their corresponding walls,

$$\mathbf{u}_{01}^{i0}(x, y' = 0) = \mathbf{u}_{01}^{i1}(x, y^* = 1) = \mathbf{0}. \tag{32}$$

The behavior of these solutions away from the walls is determined by matching. The matching procedure is algebraically complicated and so details of the solution as well as the expressions for the boundary-layer velocities and pressures are given in Appendix B. Here, we provide only the final velocity expressions for both the inner and outer approximations,

$$
u_{01}^{o}(x,y,t)=\frac{\sqrt{2}}{2}\kappa(\cos(\kappa x-t)-\sin(\kappa x-t))\times[\coth(\kappa)\sinh(\kappa y)-(\mathrm{csch}^{2}(\kappa)+\coth^{2}(\kappa))\cosh(\kappa y)]+\frac{\sqrt{2}}{\kappa}(\cos(t)
$$
$$
+\sin(t)), \tag{33a}
$$

$$
v_{01}^{o}(x,y,t)=\frac{\sqrt{2}}{2}\kappa(\cos(\kappa x-t)+\sin(\kappa x-t))\times[\coth(\kappa)\cosh(\kappa y)-(\mathrm{csch}^{2}(\kappa)+\coth^{2}(\kappa))\sinh(\kappa y)], \tag{33b}
$$

$$
u_{01}^{i0}(x,y',t)=\kappa\,\cos(\kappa x-t)y'-\frac{\sqrt{2}}{2}\kappa(\mathrm{csch}^{2}(\kappa)+\coth^{2}(\kappa))(\cos(\kappa x-t)-\sin(\kappa x-t))-\frac{\sqrt{2}}{2}\kappa(\mathrm{csch}^{2}(\kappa)
$$
$$
+\coth^{2}(\kappa))e^{-(\sqrt{2}/2)\,y'}\times\left[\cos\left(\kappa x-t+\frac{\sqrt{2}}{2}y'\right)\right.
$$
$$
\left.-\sin\left(\kappa x-t+\frac{\sqrt{2}}{2}y'\right)\right]-\frac{\sqrt{2}}{\kappa}e^{-(\sqrt{2}/2)\,y'}\left(\cos\left(\frac{\sqrt{2}}{2}y'-t\right)-\sin\left(\frac{\sqrt{2}}{2}y'-t\right)\right)+\frac{\sqrt{2}}{\kappa}(\cos(t)+\sin(t)), \tag{33c}
$$

$$
v_{01}^{i0}(x,y',t)=-\kappa\,\sin(\kappa x-t)\coth(\kappa)y'+\frac{\sqrt{2}}{2}\kappa\coth(\kappa)(\sin(\kappa x-t)+\cos(\kappa x-t))-\frac{\sqrt{2}}{2}\kappa\coth(\kappa)e^{-(\sqrt{2}/2)\,y'}
$$
$$
\times\left[\sin\left(\kappa x-t+\frac{\sqrt{2}}{2}y'\right)+\cos\left(\kappa x-t+\frac{\sqrt{2}}{2}y'\right)\right], \tag{33d}
$$

$$
u_{01}^{i1}(x,y^{*},t)=\sqrt{2}\kappa\coth(\kappa)\mathrm{csch}(\kappa)(\cos(\kappa x-t)-\sin(\kappa x-t))-\sqrt{2}\kappa\coth(\kappa)\mathrm{csch}(\kappa)e^{-(\sqrt{2}/2)(1-y^{*})}
$$
$$
\times\left(\cos\left(\kappa x-t+\frac{\sqrt{2}}{2}(1-y^{*})\right)-\sin\left(\kappa x-t+\frac{\sqrt{2}}{2}(1-y^{*})\right)\right)-\frac{\sqrt{2}}{\kappa}e^{-\sqrt{2}/2(1-y^{*})}\left(\cos\left(\frac{\sqrt{2}}{2}(1-y^{*})-t\right)\right.
$$
$$
\left.-\sin\left(\frac{\sqrt{2}}{2}(1-y^{*})-t\right)\right)+\frac{\sqrt{2}}{\kappa}(\cos(t)+\sin(t)), \tag{33e}
$$

$$
v_{01}^{i1}(x,y^{*},t)=\kappa\,\mathrm{csch}(\kappa)\sin(\kappa x-t)(1-y^{*})-\frac{\sqrt{2}}{2}\kappa\,\mathrm{csch}(\kappa)(\sin(\kappa x-t)+\cos(\kappa x-t))
$$
$$
+\frac{\sqrt{2}}{2}\kappa\,\mathrm{csch}(\kappa)e^{-(\sqrt{2}/2)(1-y^{*})}\left(\sin\left(\kappa x-t+\frac{\sqrt{2}}{2}(1-y^{*})\right)+\cos\left(\kappa x-t+\frac{\sqrt{2}}{2}(1-y^{*})\right)\right). \tag{33f}
$$

Similarly to the leading-order solution $\mathbf{u}_{00}$, we now construct a representation of $\mathbf{u}_{01}$ uniformly valid everywhere in the channel by rewriting the boundary-layer solutions in terms of the outer variable y, adding the outer and inner representations, and subtracting the overlap parts:

$$
\mathbf{u}_{01}(x,y,t)=\mathbf{u}_{01}^{o}(x,y,t)+\mathbf{u}_{01}^{i0}(x,\alpha y,t)
$$
$$
+\mathbf{u}_{01}^{i1}(x,1-\alpha(1-y),t)-\mathbf{U}_{01}(x,y,t). \tag{34}
$$

Here $\mathbf{U}_{01}(x,y,t)$, which is straightforward though tedious to derive from (33), represents the sum of all the overlap parts accounting for necessary contributions from the $O(1)$ solution. All components of $\mathbf{u}_{01}$ are periodic functions of t with a zero time-average, and consequently so is $\mathbf{u}_{01}$, which is consistent with the fact that the leading-order in ϵ flow, $\mathbf{u}_{0}=\mathbf{u}_{00}+\alpha^{-1}\mathbf{u}_{01}$, is periodic in t with a zero time average as Eqs. (11) imply. These detailed analytical

results will now be useful as we construct the $O(\epsilon)$ correction to the flow, which incorporates the nonlinear terms $(\mathbf{u}\cdot\nabla\mathbf{u})$.

IV. THE TIME-AVERAGED $O(\epsilon)$ FLOW FOR $\alpha\gg 1$

At $O(\epsilon)$ inertial effects become important and the flow, while still periodic, no longer has zero mean in time. In this section, we compute analytically the mean drift due to inertial effects. The time-averaged horizontal Eulerian drift velocity $\langle u_{1}\rangle$ is given in Eqs. (65), (68), and (70) below.

A. The structure of the solution

To determine a flow with nonzero time average, we consider the first-order correction $\mathbf{u}_{1}$ in expansion (8). We need only consider the time-averaged equations and boundary conditions

Phys. Fluids, Vol. 13, No. 7, July 2001

Peristaltically driven flows for micromixers   1845

$$\nabla^2 \langle \mathbf{u}_1 \rangle - \nabla \langle p_1 \rangle = \alpha^2 \langle \mathbf{u}_0 \cdot \nabla \mathbf{u}_0 \rangle, \quad \nabla \cdot \langle \mathbf{u}_1 \rangle = 0, \tag{35a}$$

$$\langle \mathbf{u}_1(x,0,t) \rangle = - \left\langle \cos(\kappa x - t) \frac{\partial \mathbf{u}_0}{\partial y}(x,0,t) \right\rangle, \quad \langle \mathbf{u}_1(x,1,t) \rangle = \mathbf{0}, \tag{35b}$$

where $\langle \cdot \rangle = 1/2\pi \int_0^{2\pi}(\cdot)\, dt$ denotes the time average of $(\cdot)$ over one period of the wave motion. A corresponding integral constraint,

$$\int_0^1 \langle u_1 \rangle \, dy = \frac{1}{2\pi} \int_0^{2\pi} u_0(x,0,t) \cos(\kappa x - t) \, dt = 0, \tag{36}$$

must also be applied; the vanishing integral above is exact as $u_0(x,0,t) = 0$.

Since $\mathbf{u}_0$ is known analytically for $\alpha \gg 1$ as described in Sec. III, $\langle \mathbf{u}_1 \rangle$ can be calculated. For the case of arbitrary α, we use the results in Appendix A to calculate $\langle \mathbf{u}_1 \rangle$. Here, instead, we focus on the analytical structure available for $\alpha \gg 1$. We will find (see Sec. V) that the high-frequency analytical results remain in good agreement with the full numerical results even for $\alpha \approx 10$.

To proceed, using $\mathbf{u}_0^{i0}$, the boundary-layer velocity near the moving boundary $y = 0$, the boundary condition (35b) can be shown to simplify to

$$\langle \mathbf{u}_1 \rangle (x,0) = \left(\alpha \frac{\sqrt{2}}{4} \left(\coth(\kappa) + \frac{\sin(\kappa x) - \cos(\kappa x)}{\kappa} \right) + \kappa \, \mathrm{csch}^2(\kappa) - \frac{\cos(\kappa x)}{\kappa}, 0 \right), \tag{37}$$

which consists of a part independent of x and a part periodic in x, and shows that the dimensionless velocity (in units of $\epsilon \omega h$) near the moving wall is $O(\alpha)$. Neglected terms in (37) are $O(\alpha^{-1})$. For $\kappa = O(1)$, we thus expect that the time-averaged velocity is only weakly dependent on κ. We note that expression (37) is positive for almost all values of x and κ, indicating that in almost all cases, on average, the fluid moves in the direction of the traveling wave *at* the moving wall $y = 0$. We will show, that even when at $y = 0$ the time-averaged velocity is opposite to the direction of the wave, the ''bulk'' net flow in the boundary layer near the moving boundary $y = 0$ will always be *in the direction of the wave*; i.e., for $\alpha \gg 1$ net motion opposite to the wave will be confined in a very narrow region within this boundary layer and will be insignificant in terms of fluid transport.

The nonhomogeneous terms of Eqs. (35) as well as the boundary data consist of two kinds of terms—terms independent of x and terms periodic in x. We, therefore, expect $\langle \mathbf{u}_1 \rangle$ to consist of two linearly independent parts—a part independent of x, $\langle \mathbf{U}_1 \rangle(y)$, and a part periodic in x, $\langle \mathcal{U}_1 \rangle(x,y)$, so that $\langle \mathbf{u}_1 \rangle = \langle \mathbf{U}_1 \rangle(y) + \langle \mathcal{U}_1 \rangle(x,y)$. Solutions independent of x obey the equations and the integral constraint,

$$\frac{\partial \langle V_1 \rangle}{\partial y} = 0, \tag{38a}$$

$$\frac{\partial^2 \langle U_1 \rangle}{\partial y^2} - \frac{\partial \langle P_1 \rangle}{\partial x} = \alpha^2 \langle (\mathbf{u}_0 - \mathbf{U}_0) \cdot \nabla (\mathbf{u}_0 - \mathbf{U}_0) \rangle \cdot \mathbf{e}_x, \tag{38b}$$

$$-\frac{\partial \langle P_1 \rangle}{\partial y} = \alpha^2 \langle (\mathbf{u}_0 - \mathbf{U}_0) \cdot \nabla \mathbf{u}_0 \rangle \cdot \mathbf{e}_y, \tag{38c}$$

$$\int_0^1 \langle U_1 \rangle \, dy = 0, \tag{38d}$$

where $\mathbf{U}_0 = (U_0(y,t),0)$ is the x-independent part of $\mathbf{u}_0$ [see (27) and (33)], and where $\mathbf{e}_x$ and $\mathbf{e}_y$ are unit vectors in the directions along and across the channel, respectively. It is natural to decompose the forcing $\langle \mathbf{u}_0 \cdot \nabla \mathbf{u}_0 \rangle$ as given in (38b) above, with the additional terms entering the flow periodic in x in Eqs. (42) below. Contributions that average identically to zero have been omitted. The corresponding boundary condition at the moving wall, $y = 0$, is the part of (37) independent of x,

$$\langle \mathbf{U}_1 \rangle (0) = \left(\alpha \frac{\sqrt{2}}{4} \coth(\kappa) + \kappa \, \mathrm{csch}^2(\kappa), 0 \right). \tag{39}$$

At the stationary wall, $y = 1$, the no-slip condition remains trivial,

$$\langle \mathbf{U}_1 \rangle (1) = \mathbf{0}. \tag{40}$$

From (38a), (39), and (40) it follows that

$$\langle V_1 \rangle = 0 \tag{41}$$

everywhere in the channel, i.e., there is only a nonzero time-averaged x-independent velocity along the channel. The x-periodic part of the first-order time-averaged velocity satisfies

$$\frac{\partial \langle \mathcal{U}_1 \rangle}{\partial x} + \frac{\partial \langle \mathcal{V}_1 \rangle}{\partial y} = 0, \tag{42a}$$

$$\frac{\partial^2 \langle \mathcal{U}_1 \rangle}{\partial x^2} + \frac{\partial^2 \langle \mathcal{U}_1 \rangle}{\partial y^2} - \frac{\partial \langle \mathcal{P}_1 \rangle}{\partial x} = \alpha^2 \langle \mathbf{U}_0 \cdot \nabla \mathbf{u}_0 + \mathbf{u}_0 \cdot \nabla \mathbf{U}_0 \rangle \cdot \mathbf{e}_x, \tag{42b}$$

$$\frac{\partial^2 \langle \mathcal{V}_1 \rangle}{\partial x^2} + \frac{\partial^2 \langle \mathcal{V}_1 \rangle}{\partial y^2} - \frac{\partial \langle \mathcal{P}_1 \rangle}{\partial y} = \alpha^2 \langle \mathbf{U}_0 \cdot \nabla \mathbf{u}_0 \rangle \cdot \mathbf{e}_y, \tag{42c}$$

$$\int_0^1 \langle \mathcal{U}_1 \rangle \, dy = 0, \tag{42d}$$

subject to the boundary conditions

$$\langle \mathcal{U}_1 \rangle (x,0) = \left(\alpha \frac{\sqrt{2}}{4} \left(\frac{\sin(\kappa x) - \cos(\kappa x)}{\kappa} \right) - \frac{\cos(\kappa x)}{\kappa}, 0 \right),$$

$$\langle \mathcal{U}_1 \rangle (x,1) = \mathbf{0}. \tag{43}$$

The existence of this x-periodic component of the first-order time-averaged velocity is solely due to the presence of rigid side walls at $x = \pm L/2$; if an adverse pressure gradient is applied against the pumping instead, so that net flux across a cross section of the channel is zero, the x-periodic velocity

$\langle \mathbfcal{U}_1 \rangle$ will be identically zero. The next section examines the x-independent and the x-periodic problems away from the channel walls.

B. The outer time-averaged, first-order flow for $\alpha \gg 1$

For $\alpha \gg 1$, the secondary time-averaged flow $\langle \mathbf{u}_1 \rangle$ has a boundary-layer structure with boundary layers of thickness $O(\alpha^{-1})$. Throughout most of the channel, the x-independent flow obeys the outer equations

$$\frac{\partial^2 \langle U_1^o \rangle}{\partial y^2} - \frac{\partial \langle P_1^o \rangle}{\partial x} = \alpha^2 \langle (\mathbf{u}_0^o - \mathbf{U}_0^o) \cdot \nabla \mathbf{u}_0^o \rangle \cdot \mathbf{e}_x = 0, \quad (44a)$$

$$-\frac{\partial \langle P_1^o \rangle}{\partial y} = \alpha^2 \langle (\mathbf{u}_0^o - \mathbf{U}_0^o) \cdot \nabla \mathbf{u}_0^o \rangle \cdot \mathbf{e}_y$$

$$= -\alpha^2 \frac{\kappa \, \sinh(2\kappa(1-y))}{2 \sinh^2(\kappa)}$$

$$+ \alpha \langle (\mathbf{u}_{00}^o - \mathbf{U}_{00}^o) \cdot \nabla \mathbf{u}_{01}^o \rangle \cdot \mathbf{e}_y$$

$$+ \alpha \langle (\mathbf{u}_{01}^o - \mathbf{U}_{01}^o) \cdot \nabla \mathbf{u}_{00}^o \rangle \cdot \mathbf{e}_y, \quad (44b)$$

where the right-hand sides have been computed to $O(\alpha)$ using the outer solution $\mathbf{u}_0^o = \mathbf{u}_{00}^o + \alpha^{-1} \mathbf{u}_{01}^o$. Equations (44) can be solved to arrive at the form of the velocity and pressure profiles,

$$\langle U_1^o \rangle = C_1 y^2 + C_2 y + C_3, \quad (45a)$$

$$\langle P_1^o \rangle = 2 C_1 x + P_1 - \alpha^2 \frac{\cosh(2\kappa(1-y))}{4 \sinh^2(\kappa)} + O(\alpha), \quad (45b)$$

where C_1, C_2, C_3, and P_1 are constants that cannot be determined before finding the behavior of the solution in the boundary layers. The neglected $O(\alpha)$ term in $\langle P_1^o \rangle$ above given by $\alpha \mathbf{e}_y \cdot \int_0^y \langle (\mathbf{u}_{00}^o - \mathbf{U}_{00}^o) \cdot \nabla \mathbf{u}_{01}^o + (\mathbf{u}_{01}^o - \mathbf{U}_{01}^o) \cdot \nabla \mathbf{u}_{00}^o \rangle (\bar{y}) \, d\bar{y}$ [see (44b)] is a function of y only and so does not affect x-variations in (45). The x-independent time-averaged outer flow $\langle \mathbf{U}_1^o \rangle = \langle U_1^o \rangle \mathbf{e}_x$ is in the direction along the channel only and has a parabolic profile. The pressure distribution $\langle P_1^o \rangle$ is linear in x and has a y-dependence associated with the background fluid acceleration produced by the transversely oscillating boundary. The "bulk" parabolic profile is to be expected, though a detailed calculation is necessary to determine its exact shape.

The x-periodic component of the outer time-averaged first-order velocity, $\langle \mathbfcal{U}_1^o \rangle$, satisfies the equations,

$$\frac{\partial \langle \mathcal{U}_1^o \rangle}{\partial x} + \frac{\partial \langle \mathcal{V}_1^o \rangle}{\partial y} = 0, \quad (46a)$$

$$\frac{\partial^2 \langle \mathcal{U}_1^o \rangle}{\partial x^2} + \frac{\partial^2 \langle \mathcal{U}_1^o \rangle}{\partial y^2} - \frac{\partial \langle \mathcal{P}_1^o \rangle}{\partial x} = \alpha^2 \langle \mathbf{U}_0^o \cdot \nabla \mathbf{u}_0^o \rangle \cdot \mathbf{e}_x$$

$$= \alpha^2 \frac{\sin(\kappa x)\cosh(\kappa(1-y))}{2 \sinh(\kappa)}, \quad (46b)$$

$$\frac{\partial^2 \langle \mathcal{V}_1^o \rangle}{\partial x^2} + \frac{\partial^2 \langle \mathcal{V}_1^o \rangle}{\partial y^2} - \frac{\partial \langle \mathcal{P}_1^o \rangle}{\partial y} = \alpha^2 \langle \mathbf{U}_0^o \cdot \nabla \mathbf{u}_0^o \rangle \cdot \mathbf{e}_y$$

$$= \alpha^2 \frac{\cos(\kappa x)\sinh(\kappa(1-y))}{2 \sinh(\kappa)}, \quad (46c)$$

with boundary conditions to be determined by matching with the corresponding inner solutions. We note that the right-hand side of (46b) and (46c) is curl-free, so that the stream function $\Psi(x,y)$ for this two-dimensional flow satisfies the homogeneous biharmonic equation $\nabla^4 \Psi = 0$. Consequently, the general solution to (46) is given by

$$\langle \mathcal{U}_1^o \rangle = -\text{Re}\left\{ e^{\iota \kappa x} \frac{df}{dy} \right\}, \quad \langle \mathcal{V}_1^o \rangle = \text{Re}\{\iota \kappa e^{\iota \kappa x} f(y)\}, \quad (47a)$$

$$\langle \mathcal{P}_1^o \rangle = \alpha^2 \frac{\cos(\kappa x)\cosh(\kappa(1-y))}{2\kappa \, \sinh(\kappa)} + O(\alpha), \quad (47b)$$

where $f(y) = C_4 \cosh(\kappa y) + C_5 \sinh(\kappa y) + C_6 y \cosh(\kappa y) + C_7 y \times \sinh(\kappa y)$. The complex constants C_4, C_5, C_6 and C_7 are determined by matching with the inner solutions in Sec. IV D.

The outer time-averaged first-order velocity is the sum of its x-independent and x-periodic parts, $\langle \mathbf{u}_1^o \rangle(x,y) = \langle \mathbf{U}_1^o \rangle(y) + \langle \mathbfcal{U}_1^o \rangle(x,y)$, where the last term is the result of a standing wave established by the presence of rigid side walls.

C. The inner time-averaged, first-order flow for $\alpha \gg 1$

To solve for $\langle \mathbf{u}_1 \rangle$ and $\langle p_1 \rangle$ near the walls, we rescale the transverse coordinate y as in (17), $y' = \alpha y$, $y* = 1 - \alpha(1-y)$, and evaluate the nonhomogeneous right-hand side $\langle \mathbf{u}_0 \cdot \nabla \mathbf{u}_0 \rangle$ using the inner representations of $\mathbf{u}_0$. From (45b) we expect the pressure to be $O(\alpha^2)$ and we rescale it accordingly, $\langle p_1^i \rangle' = \langle p_1^i \rangle / \alpha^2$. Neglecting terms $O(\alpha^{-1})$ and smaller, we obtain the boundary-layer equations for $\langle U_1^{i0} \rangle$ and $\langle U_1^{i1} \rangle$, the x-independent parts of the boundary-layer velocities $\langle \mathbf{u}_1^{i0} \rangle$ and $\langle \mathbf{u}_1^{i1} \rangle$,

$$\frac{\partial^2 \langle U_1^{i0} \rangle}{\partial y'^2} - \frac{\partial \langle P_1^{i0} \rangle'}{\partial x} = \alpha \left\langle v_{00}^{i0} \frac{\partial(u_{00}^{i0} - U_{00}^{i0})}{\partial y'} \right\rangle$$

$$+ \left\langle v_{00}^{i0} \frac{\partial(u_{01}^{i0} - U_{01}^{i0})}{\partial y'} \right.$$

$$+ v_{01}^{i0} \frac{\partial(u_{00}^{i0} - U_{00}^{i0})}{\partial y'} \right\rangle, \quad (48a)$$

$$\frac{\partial \langle P_1^{i0} \rangle'}{\partial y'} = O(\alpha^{-1}), \quad (48b)$$

$$\frac{\partial^2 \langle U_1^{i1} \rangle}{\partial y*^2} - \frac{\partial \langle P_1^{i1} \rangle'}{\partial x} = \left\langle v_{01}^{i1} \frac{\partial(u_{00}^{i1} - U_{00}^{i1})}{\partial y*} \right\rangle, \quad (48c)$$

Phys. Fluids, Vol. 13, No. 7, July 2001

Peristaltically driven flows for micromixers   1847

$$\frac{\partial \langle P_1^{i1} \rangle'}{\partial y^*} = O(\alpha^{-2}), \tag{48d}$$

where all quantities in brackets on the right-hand side are $O(1)$ and can be evaluated analytically, though the expressions are long and cumbersome to write. Since $\langle V_1 \rangle = 0$ and $\langle U_1 \rangle$ is independent of x, the continuity equation is automatically satisfied. The right-hand sides of (48) are functions of y' or y^* only, since time-averaging eliminates the x-dependence from the expressions above as well. At leading order, the pressures $\langle P_1^{i0} \rangle'$ and $\langle P_1^{i1} \rangle'$ are at most functions of x. However, since far from the walls, we require that the boundary-layer velocities are finite, we conclude that

$$\frac{\partial \langle P_1^{i0} \rangle'}{\partial x} = 0, \quad \frac{\partial \langle P_1^{i1} \rangle'}{\partial x} = 0, \tag{49}$$

or

$$\langle P_1^{i0} \rangle'(y') = P_1^{i0} + O(\alpha^{-1}), \quad \langle P_1^{i1} \rangle'(y^*) = P_1^{i1} + O(\alpha^{-2}), \tag{50}$$

where P_1^{i0} and P_1^{i1} are constants. We require that each boundary-layer velocity satisfies the appropriate boundary condition at the walls,

$$\langle U_1^{i0} \rangle|_{y'=0} = \alpha \frac{\sqrt{2}}{4} \coth(\kappa) + \kappa \, \operatorname{csch}^2(\kappa), \quad \langle U_1^{i1} \rangle|_{y^*=1} = 0. \tag{51}$$

Equations (48) can be integrated with respect to y' or y^* to arrive at boundary-layer velocities of the form

$$\langle U_1^{i0} \rangle(y') = \alpha \left(H_{x0}^{i0}(y') + \frac{\sqrt{2}}{4} \coth(\kappa) \right) + H_{x1}^{i0}(y') + \kappa \, \operatorname{csch}^2(\kappa), \tag{52a}$$

$$\langle U_1^{i1} \rangle(y^*) = H_{x1}^{i1}(y^*), \tag{52b}$$

where the H's are functions that can be calculated explicitly (we accomplished this using the symbolic mathematics package *Maple*),

$$H_{x0}^{i0}(y') = \int_0^{y'} \int_\infty^{\bar{y}} \left\langle v_{00}^{i0} \frac{\partial(u_{00}^{i0} - U_{00}^{i0})}{\partial y'} \right\rangle (s) \, ds \, d\bar{y}, \tag{53a}$$

$$H_{x1}^{i0}(y') = \int_0^{y'} \int_\infty^{\bar{y}} \left\langle v_{00}^{i0} \frac{\partial(u_{01}^{i0} - U_{01}^{i0})}{\partial y'} + v_{01}^{i0} \frac{\partial(u_{00}^{i0} - U_{00}^{i0})}{\partial y'} \right\rangle \times (s) \, ds \, d\bar{y}, \tag{53b}$$

$$H_{x1}^{i1}(y^*) = \int_1^{y^*} \int_{-\infty}^{\bar{y}} \left\langle v_{01}^{i1} \frac{\partial(u_{00}^{i1} - U_{00}^{i1})}{\partial y^*} \right\rangle (s) \, ds \, d\bar{y}. \tag{53c}$$

The time-averaged x-independent velocites $\langle U_1^{i0} \rangle(y')$ and $\langle U_1^{i1} \rangle(y^*)$ are completely determined by (52) and (53). The

time-averaged velocity in the boundary layer near $y=0$, $\langle U_1^{i0} \rangle$, consists of a dominant $O(\alpha)$ part and a smaller $O(1)$ contribution,

$$\langle U_1^{i0} \rangle = \alpha \langle U_{10}^{i0} \rangle + \langle U_{11}^{i0} \rangle. \tag{54}$$

Both terms are important for calculating the net parabolic outer flow and constructing a solution valid uniformly everywhere in the channel.

The first-order time-averaged x-periodic velocity $\langle \mathcal{U}_1^{i0} \rangle$ satisfies the boundary-layer equations (again, the pressure has been rescaled as indicated at the beginning of this subsection)

$$\frac{\partial \langle \mathcal{U}_1^{i0} \rangle}{\partial x} + \alpha \frac{\partial \langle \mathcal{V}_1^{i0} \rangle}{\partial y'} = 0, \tag{55a}$$

$$\frac{\partial^2 \langle \mathcal{U}_1^{i0} \rangle}{\partial y'^2} - \frac{\partial \langle \mathcal{P}_1^{i0} \rangle'}{\partial x}$$
$$= \alpha \left\langle v_{00}^{i0} \frac{\partial U_{00}^{i0}}{\partial y'} \right\rangle + \left\langle v_{00}^{i0} \frac{\partial U_{01}^{i0}}{\partial y'} + v_{01}^{i0} \frac{\partial U_{00}^{i0}}{\partial y'} + U_{00}^{i0} \frac{\partial u_{00}^{i0}}{\partial x} \right\rangle, \tag{55b}$$

$$\frac{\partial \langle \mathcal{P}_1^{i0} \rangle'}{\partial y'} = O(\alpha^{-1}), \tag{55c}$$

$$\frac{\partial \langle \mathcal{U}_1^{i1} \rangle}{\partial x} + \alpha \frac{\partial \langle \mathcal{V}_1^{i1} \rangle}{\partial y^*} = 0, \tag{55d}$$

$$\frac{\partial^2 \langle \mathcal{U}_1^{i1} \rangle}{\partial y^{*2}} - \frac{\partial \langle \mathcal{P}_1^{i1} \rangle'}{\partial x} = \left\langle v_{01}^{i1} \frac{\partial U_{00}^{i1}}{\partial y^*} + U_{00}^{i1} \frac{\partial u_{00}^{i1}}{\partial x} \right\rangle, \tag{55e}$$

$$\frac{\partial \langle \mathcal{P}_1^{i1} \rangle'}{\partial y^*} = O(\alpha^{-2}), \tag{55f}$$

where, again, the right-hand sides can be evaluated analytically and we have done so using the symbolic package *Maple*. The time-averaged right-hand sides are functions periodic in x and consist of two types of terms: terms independent of y and terms exponentially small in y as we go far from the walls. Since the fluid velocities $\langle \mathcal{U}_1^{i0} \rangle(x,y)$ and $\langle \mathcal{U}_1^{i1} \rangle(x,y)$ must be finite away from the walls, the terms independent of y on the right-hand side can only contribute to the pressure gradient. Conversely, since at leading order the pressures $\langle \mathcal{P}_1^{i0} \rangle'$ and $\langle \mathcal{P}_1^{i1} \rangle'$ are functions of at most x, it must be true that the pressure gradients above exactly equal the terms on the right-hand side that are independent of y,

$$\frac{\partial \langle \mathcal{P}_1^{i0} \rangle'}{\partial x} = -\frac{1}{2} \coth(\kappa) \sin(\kappa x) + O(\alpha^{-1}),$$
$$\frac{\partial \langle \mathcal{P}_1^{i1} \rangle'}{\partial x} = -\frac{1}{2} \operatorname{csch}(\kappa) \sin(\kappa x) + O(\alpha^{-2}). \tag{56}$$

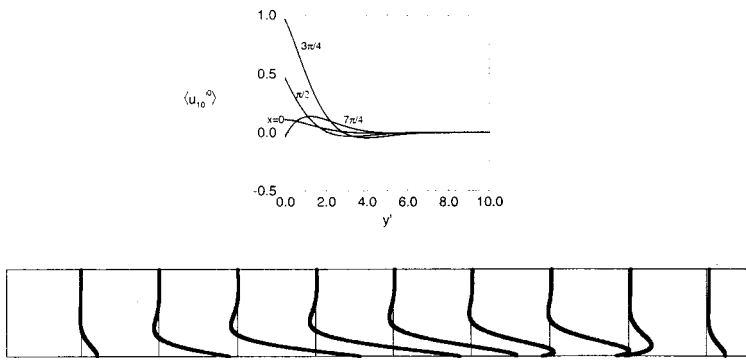We thus have for the pressure distribution in the boundary layers,

FIG. 5. Velocity profiles given by Eqs. (52a), (54), (59a), and (61) of the $O(\alpha)$ steady, traveling-wave-driven flow in a long, closed channel in the boundary layer near the oscillating wall $y=0$. $\langle u_{10}^{i0} \rangle$ denotes the velocity component along the channel and y' denotes the inner coordinate measured from the moving boundary. Several representative choices of x are shown in the upper figure: $x=0$, $\pi/2$, $3\pi/4$ and $7\pi/4$; $\kappa=1$. The schematic below shows the behavior of these velocity profiles at different positions along the channel over one wavelength of the driving wave (positive x is to the right).

$$\langle \mathcal{P}_1^{i0} \rangle' = \frac{1}{2\kappa} \coth(\kappa)\cos(\kappa x)+O(\alpha^{-1}),$$

$$\langle \mathcal{P}_1^{i1} \rangle' = \frac{1}{2\kappa} \operatorname{csch}(\kappa)\cos(\kappa x)+O(\alpha^{-2}). \tag{57}$$

We require that each boundary-layer velocity satisfies the appropriate boundary condition at the walls,

$$\langle \mathcal{U}_1^{i0} \rangle|_{y'=0} = \alpha \frac{\sqrt{2}}{4\kappa}(\sin(\kappa x)-\cos(\kappa x)) - \frac{\cos(\kappa x)}{\kappa},$$

$$\langle \mathcal{U}_1^{i1} \rangle|_{y*=1} = 0, \tag{58a}$$

$$\langle \mathcal{V}_1^{i0} \rangle|_{y'=0} = 0, \langle \mathcal{V}_1^{i1} \rangle|_{y*=1} = 0. \tag{58b}$$

Equations (55b) and (55e) can then be integrated with respect to y' and $y*$ to arrive at boundary-layer velocities of a form similar to the x-independent solution $\langle U_1^i \rangle$,

$$\langle \mathcal{U}_1^{i0} \rangle(x,y') = \alpha \left(\mathcal{H}_{x0}^{i0}(x,y') + \frac{\sqrt{2}}{4\kappa}(\sin(\kappa x)-\cos(\kappa x)) \right)$$

$$+ \mathcal{H}_{x1}^{i0}(x,y') - \frac{\cos(\kappa x)}{\kappa}, \tag{59a}$$

$$\langle \mathcal{U}_1^{i1} \rangle(x,y*) = \mathcal{H}_{x1}^{i1}(x,y*), \tag{59b}$$

where the $\mathcal{H}$'s are functions that can be calculated explicitly, and we have done so using *Maple*,

$$\mathcal{H}_{x0}^{i0}(x,y') = \int_0^{y'} \int_\infty^{\bar{y}} \left\langle v_{00}^{i0} \frac{\partial U_{00}^{i0}}{\partial y'} \right\rangle(x,s)\,ds\,d\bar{y}, \tag{60a}$$

$$\mathcal{H}_{x1}^{i0}(x,y') = \int_0^{y'} \int_\infty^{\bar{y}} \left[\left\langle v_{00}^{i0}\frac{\partial U_{01}^{i0}}{\partial y'} + v_{01}^{i0}\frac{\partial U_{00}^{i0}}{\partial y'} + U_{00}^{i0}\frac{\partial u_{00}^{i0}}{\partial x} \right\rangle \right.$$

$$\left. \times(x,s) - \frac{1}{2}\coth(\kappa)\sin(\kappa x) \right] ds\,d\bar{y}, \tag{60b}$$

$$\mathcal{H}_{x1}^{i1}(x,y*) = \int_1^{y*} \int_{-\infty}^{\bar{y}} \left[\left\langle v_{01}^{i1}\frac{\partial U_{00}^{i1}}{\partial y*} + U_{00}^{i1}\frac{\partial u_{00}^{i1}}{\partial x} \right\rangle(x,s) \right.$$

$$\left. - \frac{1}{2}\operatorname{csch}(\kappa)\sin(\kappa x) \right] ds\,d\bar{y}. \tag{60c}$$

The time-averaged x-periodic velocites $\langle \mathcal{U}_1^{i0} \rangle$ and $\langle \mathcal{U}_1^{i1} \rangle$ are completely determined by (59) and (60). The time-averaged

x-periodic horizontal velocity in the boundary layer near $y=0$ has a similar structure to the x-independent velocity there—it consists of a dominant $O(\alpha)$ part and a smaller $O(1)$ contribution,

$$\langle \mathcal{U}_1^{i0} \rangle = \alpha\langle \mathcal{U}_{10}^{i0} \rangle + \langle \mathcal{U}_{11}^{i0} \rangle. \tag{61}$$

The corresponding transverse velocities $\langle \mathcal{V}_1^{i0} \rangle$ and $\langle \mathcal{V}_1^{i1} \rangle$ can be computed by integrating the continuity equation in each boundary layer. Since the transverse velocities are an order of magnitude (in α) smaller than the corresponding longitudinal velocities, only the transverse velocity in the boundary layer near the moving boundary is significant ($O(1)$),

$$\langle \mathcal{V}_1^{i0} \rangle(x,y') = \int_0^{y'} \frac{\partial\langle \mathcal{U}_{10}^{i0} \rangle}{\partial x}(x,s)\,ds + O(\alpha^{-1}),$$

$$\langle \mathcal{V}_1^{i1} \rangle(x,y*) = O(\alpha^{-1}). \tag{62}$$

The time-averaged first-order inner velocities are the sum of their x-independent and x-periodic parts, $\langle \mathbf{u}_1^i \rangle(x,y) = \langle \mathbf{U}_1^i \rangle(y) + \langle \mathcal{U}_1^i \rangle(x,y)$.

Graphs of $\langle u_{10}^{i0} \rangle, \langle u_{11}^{i0} \rangle$, and $\langle u_1^{i1} \rangle$ are shown in Figs. 5 and 6. They clearly show that the dominant $O(\alpha)$ net Eulerian velocity in the boundary layer near the oscillating wall is *in the direction of the driving wave*. Also, the dominant flow, $\langle u_{10}^{i0} \rangle$, is confined near the moving wall and is zero away from it. The $O(1)$ correction to this flow, $\langle u_{11}^{i0} \rangle$, displays an oscillatory behavior near the moving wall and may be opposite to the wave—insufficiently so, however, to cause net ''bulk'' fluid motion opposite to the wave in this boundary layer. The net flow near the stationary wall, $\langle u_1^{i1} \rangle$, is, for most positions x along the channel, in the direction of the wave (see also the discussion in Sec. IV D), but may run opposite to it at some positions x along the channel. The flow in this boundary layer displays typical boundary-layer behavior—a uniform flow away from the wall decreasing quickly to zero as we approach the wall ($y*=1$).

D. Completing the solution

Having determined the boundary-layer behavior, we return to (45a) and (47a) and evaluate the undetermined constants. These are determined by matching the outer and inner velocities. We do so separately for the x-independent and the x-periodic velocities.
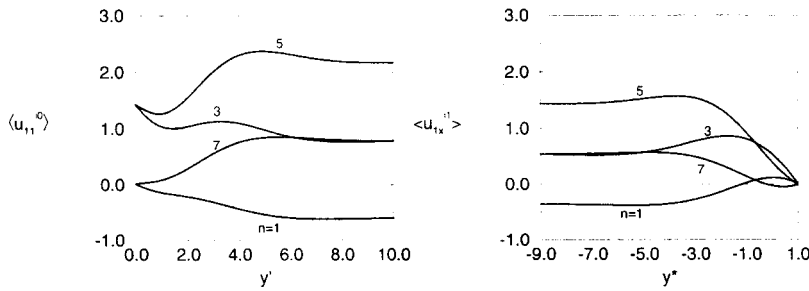
FIG. 6. Velocity profiles given by Eqs. (52), (54), (59), and (61) of the $O(1)$, steady, traveling-wave-driven flow in a long, closed channel in the boundary layers near the two walls. $\langle u_1^i \rangle$ denotes the velocity component along the channel and y' and y^* denote the boundary-layer coordinates; $\kappa = 1$. We have plotted these velocities at different positions along the channel ($x = n\pi/4$) to demonstrate the difference in fluid behavior for different longitudinal positions x.

The boundary conditions that the x-independent net outer velocity $\langle U_1^o \rangle$ must satisfy are

$$\langle U_1^o \rangle(0) = \lim_{y' \to \infty} \langle U_1^{i0} \rangle = \tfrac{1}{4}\kappa \coth^2(\kappa) + \tfrac{1}{2}\kappa \, \mathrm{csch}^2(\kappa), \tag{63a}$$

$$\langle U_1^o \rangle(1) = \lim_{y^* \to -\infty} \langle U_1^{i1} \rangle = \tfrac{3}{4}\kappa \, \mathrm{csch}^2(\kappa), \tag{63b}$$

which establishes two of the three unknown constants in the expression for the outer velocity (45a),

$$C_3 = \tfrac{1}{4}\kappa \coth^2(\kappa) + \tfrac{1}{2}\kappa \, \mathrm{csch}^2(\kappa), \quad C_2 = -\tfrac{1}{4}\kappa - C_1. \tag{64}$$

Finally, the constant C_1 can be found by imposing the zero flux condition (36) (the channel is closed at both ends). It is necessary first, however, to compute a representation of $\langle U_1 \rangle$ valid uniformly everywhere in the channel (Fig. 7).

Adding the outer and inner representations of $\langle U_1 \rangle$ and subtracting the overlapping parts, we obtain

$$\langle U_1 \rangle(y) = \langle U_1^o \rangle(y) + \langle U_1^{i0} \rangle(\alpha y) + \langle U_1^{i1} \rangle(1 - \alpha(1-y))$$
$$- \lim_{y' \to \infty} \langle U_1^{i0} \rangle(y') - \lim_{y^* \to -\infty} \langle U_1^{i1} \rangle(y^*)$$
$$= C_1 y^2 - \left(\tfrac{1}{4}\kappa + C_1 \right) y + \alpha \frac{\sqrt{2}}{4} \coth(\kappa)$$
$$+ \kappa \, \mathrm{csch}^2(\kappa) + \alpha H_{x0}^{i0}(\alpha y) + H_{x1}^{i0}(\alpha y)$$
$$+ H_{x1}^{i1}(1 - \alpha(1-y)) - \tfrac{3}{4}\kappa \, \mathrm{csch}^2(\kappa). \tag{65}$$

The condition of zero net flux across a cross section of the channel requires that
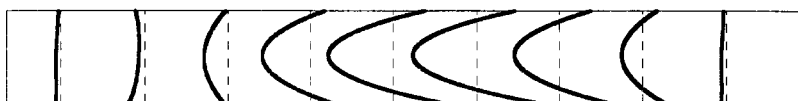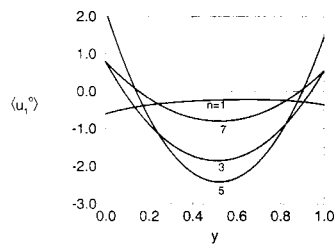
$$\int_0^1 \langle U_1 \rangle(y) dy = -\frac{C_1}{6} + \frac{5}{8}\kappa \, \mathrm{csch}^2(\kappa) + \frac{1}{8}\kappa \coth^2(\kappa)$$
$$+ \frac{1}{2}\coth(\kappa) + O(\alpha^{-1}) = 0, \tag{66}$$

where we have used the results

$$\int_0^\infty \alpha \left(H_{x0}^{i0}(\alpha y) + \frac{\sqrt{2}}{4}\coth(\kappa) \right) dy = \frac{1}{2}\coth(\kappa), \tag{67a}$$

$$\int_0^\infty \left(H_{x1}^{i0}(\alpha y) - \tfrac{1}{4}\kappa \coth^2(\kappa) - \tfrac{1}{2}\kappa \, \mathrm{csch}^2(\kappa) \right) dy = O(\alpha^{-1}), \tag{67b}$$

$$\int_0^\infty \left(H_{x1}^{i1}(1 - \alpha(1-y)) - \tfrac{3}{4}\kappa \, \mathrm{csch}^2(\kappa) \right) dy = O(\alpha^{-1}). \tag{67c}$$

These results allow us to solve for the remaining constant C_1. We obtain

$$C_1 = 3\coth(\kappa) + \tfrac{15}{4}\kappa \, \mathrm{csch}^2(\kappa) + \tfrac{3}{4}\coth^2(\kappa), \tag{68a}$$

$$C_2 = -3\coth(\kappa) - \tfrac{7}{2}\kappa \, \mathrm{csch}^2(\kappa) - \kappa \coth^2(\kappa), \tag{68b}$$

where contributions $O(\alpha^{-1})$ and smaller are neglected. We note that the constants C_1, C_2 and C_3 describing the parabolic outer flow are $O(1)$. In other words, the x-independent return flow in the middle of the channel is independent of α and the velocity profile approaches a parabola.

Finally, the x-periodic net outer velocity is subject to the boundary conditions

FIG. 7. Velocity profiles given by Eqs. (45a) and (47a) for the parabolic outer return flow away from the walls. $\langle u_1^o \rangle = \langle U_1^o \rangle + \langle \mathcal{U}_1^o \rangle$ denotes the velocity component along the channel and y denotes the coordinate across the channel; $x = n\pi/4$, $\kappa = 1$. The schematic shows the distribution of the horizontal outer velocities as a function of the longitudinal coordinate x over one wavelength of the driving wave.
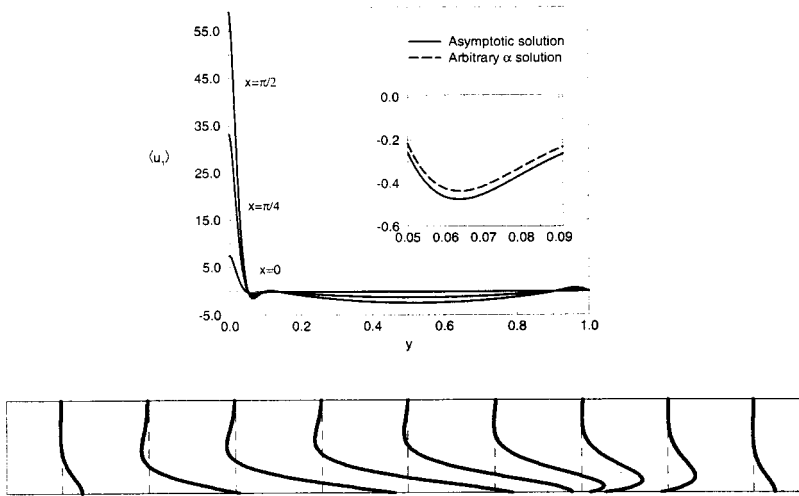
FIG. 8. Velocity profiles for the steady, traveling-wave-driven flow in a long, closed channel; $\alpha = 70$; $\kappa = 1$. $\langle u_1 \rangle$ denotes the velocity component along the channel and y denotes the coordinate across the channel. The plot above shows the asymptotic solution for $\alpha \gg 1$ (solid curve), as well as the complete solution for an arbitrary α (dashed curve). The two superpose on the large graph, and the inset illustrates the small difference. Several characteristic values of x are shown, $x = 0$, $x = \pi/4$ and $x = \pi/2$. The schematic below illustrates the behavior of this velocity in the boundary layer near the oscillating wall at different positions along the channel.

$$\lim_{y \to 0} \langle \mathcal{U}_1^o \rangle (x,y) = \lim_{y' \to \infty} \langle \mathcal{U}_1^{i0} \rangle$$
$$= -\tfrac{3}{4} \coth(\kappa) \{ \cos(\kappa x) + \sin(\kappa x) \}, \qquad (69a)$$

$$\lim_{y \to 1} \langle \mathcal{U}_1^o \rangle (x,y) = \lim_{y^* \to -\infty} \langle \mathcal{U}_1^{i1} \rangle$$
$$= -\tfrac{3}{4} \operatorname{csch}(\kappa) \{ \cos(\kappa x) + \sin(\kappa x) \}, \qquad (69b)$$

$$\lim_{y \to 0} \langle \mathcal{V}_1^o \rangle (x,y) = \lim_{y' \to \infty} \langle \mathcal{V}_1^{i0} \rangle$$
$$= -\tfrac{1}{2} \sin(\kappa x) + \tfrac{3}{4} \kappa \coth(\kappa) \{ \cos(\kappa x)$$
$$- \sin(\kappa x) \} y, \qquad (69c)$$

$$\lim_{y \to 1} \langle \mathcal{V}_1^o \rangle (x,y) = \lim_{y^* \to -\infty} \langle \mathcal{V}_1^{i1} \rangle$$
$$= \tfrac{3}{4} \kappa \operatorname{csch}(\kappa) \{ \cos(\kappa x) - \sin(\kappa x) \} (y-1).$$
$$\qquad (69d)$$

These are sufficient for determining the four unknown constants $C_4 - C_7$ of (47a). We have computed these using *Maple*, but since they are long and cumbersome to write, we do not present them here. The flux integral constraint (42d) is automatically satisfied. Adding the outer and inner representations of $\langle \mathcal{U}_1 \rangle$ and $\langle \mathcal{V}_1 \rangle$ and subtracting the overlapping parts, we obtain

$$\langle \mathcal{U}_1 \rangle (x,y) = \langle \mathcal{U}_1^o \rangle (x,y) + \langle \mathcal{U}_1^{i0} \rangle (\alpha y) + \langle \mathcal{U}_1^{i1} \rangle (1 - \alpha(1-y))$$
$$- \lim_{y' \to \infty} \langle \mathcal{U}_1^{i0} \rangle (y') - \lim_{y^* \to -\infty} \langle \mathcal{U}_1^{i1} \rangle (y^*)$$
$$= -\operatorname{Re} \left\{ e^{\iota \kappa x} \frac{df}{dy} \right\} + \alpha \left(\mathcal{H}_{x0}^{i0}(x, \alpha y) \right.$$
$$+ \frac{\sqrt{2}}{4\kappa} (\sin(\kappa x) - \cos(\kappa x)) \right) + \mathcal{H}_{x1}^{i0}(x, \alpha y)$$
$$- \frac{\cos(\kappa x)}{\kappa} + \mathcal{H}_{x1}^{i1}(x, 1 - \alpha(1-y)) + \tfrac{3}{4} \{ \coth(\kappa)$$
$$+ \operatorname{csch}(\kappa) \} \{ \cos(\kappa x) + \sin(\kappa x) \} + O(\alpha^{-1}),$$
$$\qquad (70a)$$

$$\langle \mathcal{V}_1 \rangle (x,y) = \langle \mathcal{V}_1^o \rangle (x,y) + \langle \mathcal{V}_1^{i0} \rangle (\alpha y) + \langle \mathcal{V}_1^{i1} \rangle (1 - \alpha(1-y))$$
$$- \lim_{y' \to \infty} \langle \mathcal{V}_1^{i0} \rangle (y') - \lim_{y^* \to -\infty} \langle \mathcal{V}_1^{i1} \rangle (y^*)$$
$$= \operatorname{Re} \{ \iota \kappa e^{\iota \kappa x} f(y) \} + \int_0^{\alpha y} \frac{\partial \langle \mathcal{U}_{10}^{i0} \rangle}{\partial x} (x,s) \, ds + \tfrac{1}{2} (\kappa x)$$
$$- \tfrac{3}{4} \kappa \coth(\kappa) \{ \cos(\kappa x) - \sin(\kappa x) \} y$$
$$- \tfrac{3}{4} \kappa \operatorname{csch}(\kappa) \{ \cos(\kappa x) - \sin(\kappa x) \} (y-1)$$
$$+ O(\alpha^{-1}), \qquad (70b)$$

where $f(y)$ is given in (47a). The first-order, time averaged velocity is the sum of its time-independent and time-periodic parts, $\langle \mathbf{u}_1 \rangle (x,y) = \langle \mathbf{U}_1 \rangle (y) + \langle \mathcal{U}_1 \rangle (x,y)$.

A graph of the first-order, time-averaged velocity $\langle u_1 \rangle$ valid uniformly everywhere in the channel is shown in Fig. 8, superimposed on the graph of the exact solution that is numerically calculated for any α as described in Appendix A. The asymptotic solution closely approximates the exact solution for the chosen value $\alpha = 70$. The analytic results that allow the construction of Fig. 8 are one of the main contributions of this paper.

V. SUMMARY OF IMPORTANT FLOW FEATURES

Several features of the net flow $\langle u_1 \rangle$ should be emphasized. For $\alpha \gg 1$:

(i)   The time-averaged net Eulerian velocity consists of two components—an ''underlying'' component independent of position x, and a superposed component periodic in x; the latter is a standing wave flow resulting from the presence of rigid side walls in the channel.

(ii)   The x-independent flow is dominant for a driving wave with a short dimensionless wavelength ($\kappa \gg 1$); the x-periodic flow is dominant for a driving wave with a long wavelength ($\kappa \ll 1$). The two com-
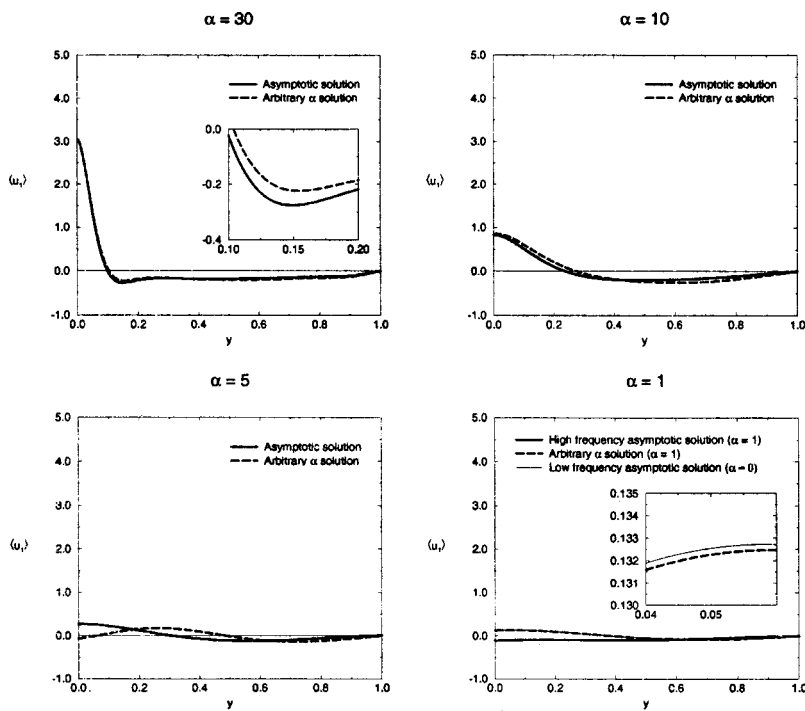
FIG. 9. Velocity profiles of the steady, traveling-wave-driven flow in a long, closed channel for $\alpha = 30$, 10, 5 and 1; $x=0$, $\kappa=1$. $\langle u_1 \rangle$ denotes the velocity component along the channel and y denotes the coordinate across the channel. The first three graphs compare the exact solution to the high-frequency asymptotic solution developed in this paper. The last graph compares the exact solution for $\alpha=1$ to a low-frequency ($\alpha = 0$) asymptotic result, Eq. (71).

ponents are comparable for moderate wavelengths $\kappa \approx O(1)$.

(iii)   The (Eulerian) time-averaged velocity along the channel in a boundary layer of thickness $O(h\alpha^{-1})$ near the oscillating boundary is *in the direction of the traveling wave* for $\kappa = O(1)$ and is $O(\alpha\epsilon^2\omega h)$.

(iv)   The return flow in a closed channel is *opposite to the direction of the driving wave* and consists of an x-independent pressure-driven Poiseuille flow superposed to a x-periodic return flow caused by the presence of rigid side walls in the channel. For $\alpha \gg 1$, the return flow is independent of α and has velocities $O(\epsilon^2\omega h)$.

(v)   A boundary layer of thickness $O(\alpha^{-1}h)$ near the stationary boundary may exhibit a small $O(\epsilon^2\omega h)$ reversal in the local fluid speed directed opposite to the bulk return flow away from the walls.

Features (i)–(iv) are consistent with a laboratory scale experiment, which was designed to examine $\alpha \gg 1$, as described in Appendix C.

It is appropriate to attempt a physical explanation of the net velocity distribution obtained above. On average, near the moving wall, fluid is trapped in the traveling wave and is consequently propagating *in the direction of the wave*. This net flow is similar to a shear flow due to a boundary translating with a constant velocity. Due to the small amplitude motion of the wall and the high frequency ($\alpha \gg 1$), this effect takes place only in a thin boundary-layer region near the moving wall. Since the channel is closed, there is a return flow in the bulk *opposite to the driving wave* due to mass conservation. The rigid side walls in the channel cause the establishment of a standing wave which, for small κ (large

wavelengths), is dominant and imposes a spatially-periodic structure of the flow. Near the stationary wall which is parallel to the moving wall, the fluid responds to the motion in the bulk by generally going opposite to it to try to locally conserve mass; this results in its net motion *in the direction of the wave*, i.e., opposite to the return flow in the bulk. This response is not necessarily always present, however; for some positions x along the channel, the net flow in this boundary layer may be in the direction of the bulk flow, which is a consequence of the standing wave flow.

The asymptotic solution described above, while developed for the high-frequency limit $\alpha \gg 1$, gives correct net velocity representations even for relatively small α. Comparison of this asymptotic solution with the solution for arbitrary α is shown on the first three graphs of Fig. 9 for $\alpha = 30, 10$, and 5. The high-frequency asymptotic solution approximates the exact solution closely for values as low as $\alpha = 10$ for $\kappa = O(1)$. For larger κ, the asymptotic solution requires higher values of α to provide a good approximation to the exact solution. The lowest value of α for which the high-frequency asymptotic solution is valid scales roughly linearly with κ for $\kappa > 3$.

At low frequencies, the net Eulerian velocity $\langle u_1 \rangle$ is independent of α. It is important to recognize that the net Eulerian velocity can differ substantially from the net Lagrangian velocity of a fluid particle; the latter indicates the actual transport of fluid particles and is discussed in Sec. VI. A good approximation to the exact solution for low values of α is given by the low-frequency ($\alpha=0$) result [solve Eq. (11) with $\alpha=0$]

$$\langle u_1\rangle(y) = \frac{\kappa(\sinh^2(\kappa)+\kappa^2)}{2(\sinh^2(\kappa)-\kappa^2)}(3y^2-4y+1)$$

$$+\frac{3\cos(\kappa x)}{\kappa(\sinh^2(\kappa)-\kappa^2)}\{(\kappa^2-\sinh^2(\kappa))\cosh(\kappa y)$$

$$-\kappa\,\sinh^2(\kappa)y\,\sinh(\kappa y)+(\sinh(\kappa)\cosh(\kappa)-\kappa)$$

$$\times\sinh(\kappa y)+(\kappa\,\cosh(\kappa)\sinh(\kappa)$$

$$-\kappa)y\,\cosh(\kappa y)\},\tag{71a}$$

$$\langle v_1\rangle(x,y)=\frac{3\sin(\kappa x)}{(\sinh^2(\kappa)-\kappa^2)}\}\kappa\,\sinh(\kappa y)-\sinh^2(\kappa)y$$

$$\times\cosh(\kappa y)+(\cosh(\kappa)\sinh(\kappa)-\kappa)$$

$$\times y\,\sinh(\kappa y)\}.\tag{71b}$$

The last graph of Fig. 9 shows a comparison of the exact solution for $\alpha=1$ with this low-frequency asymptotic solution. For $0\leqslant\alpha<1$, this low-frequency asymptotic solution is in excellent agreement with the exact numerical solution.

VI. PARTICLE PATHS: EULERIAN VS LAGRANGIAN VELOCITIES

In this section we supplement our discussion of the Eulerian description of the peristaltically driven motion with a Lagrangian description of the average velocities of individual fluid particles. The calculation is similar to the corresponding analysis for the paths of particles in water-wave problems. With the Eulerian velocity $\mathbf{u}(x,y,t)$ known, the position $\mathbf{X}(t)=(X(t),Y(t))$ of a given fluid particle as a function of time can be found by integrating the differential equations [the choice of dimensional scales was given in Sec. II and explains the appearance of ϵ in Eqs. (72)],

$$\frac{d\mathbf{X}(t)}{dt}=\epsilon\mathbf{u}(X(t),Y(t),t),\tag{72}$$

subject to the initial condition

$$\mathbf{X}(0)=\mathbf{X}_0=(X_0,Y_0).\tag{73}$$

If the initial position $\mathbf{X}_0$ of a particle is used as a label, then the path of a particle will be given by $\mathbf{X}(t|\mathbf{X}_0)$, and its *Lagrangian* velocity will be given by $\mathbf{u}^L=(d\mathbf{X}/dt)(t|\mathbf{X}_0)$.

It is clear from (72) that $\mathbf{X}(t)$ can be written as a power series in ϵ and so can the Lagrangian velocity $\mathbf{u}^L(t)=d\mathbf{X}/dt$,

$$\mathbf{X}(t)=\mathbf{X}_0+\epsilon\mathbf{X}_1(t)+\epsilon^2\mathbf{X}_2(t)+O(\epsilon^3)\ldots,\tag{74a}$$

$$\mathbf{u}^L(t)=\epsilon\mathbf{u}_1^L(t)+\epsilon^2\mathbf{u}_2^L(t)+O(\epsilon^3)\cdots.\tag{74b}$$

Since $\epsilon\ll1$, $|\mathbf{X}-\mathbf{X}_0|=O(\epsilon)\ll1$ at all times during one period of the oscillation, and we can expand the Eulerian velocity $\mathbf{u}(X(t),Y(t),t)$ in a Taylor series around the initial position $\mathbf{X}_0$,

$$\mathbf{u}(\mathbf{X}(t),t)=\mathbf{u}|_{\mathbf{X}=\mathbf{X}_0}+(\mathbf{X}-\mathbf{X}_0)\cdot\nabla\mathbf{u}|_{\mathbf{X}=\mathbf{X}_0}+O(\epsilon^2)\ldots.\tag{75}$$

It should be noted that (75) requires that $\epsilon\alpha\ll1$ to correctly represent the behavior of $\mathbf{u}(X(t),Y(t),t)$ in the boundary layers, where velocity gradients are $O(\alpha)$ when $\alpha\gg1$. This requirement can be relaxed away from the walls, where $\epsilon\ll1$ is sufficient. Using (8), the perturbation expansion of $\mathbf{u}$ previously employed, and keeping terms up to $O(\epsilon)$, Eqs. (75) becomes

$$\mathbf{u}(X(t),Y(t),t)=\mathbf{u}_0|_{\mathbf{X}=\mathbf{X}_0}+\epsilon\mathbf{u}_1|_{\mathbf{X}=\mathbf{X}_0}+\mathbf{X}_1\cdot\nabla\mathbf{u}_0|_{\mathbf{X}=\mathbf{X}_0}(t)$$

$$+O(\epsilon^2)\cdots.\tag{76}$$

Equation (76) is then used in (72) and the resulting problem is examined separately at each order in ϵ. At leading order, we use (19), so the Lagrangian problem is

$$u_1^L(t)=\frac{dX_1}{dt}=(u_{00}(X_0,Y_0,t)+\alpha^{-1}u_{01}(X_0,Y_0,t)),\tag{77a}$$

$$v_1^L(t)=\frac{dY_1}{dt}=(v_{00}(X_0,Y_0,t)+\alpha^{-1}v_{01}(X_0,Y_0,t)).\tag{77b}$$

Since the right-hand sides of (77) are periodic functions of t with zero mean, time-averaging (77) confirms the expected result that at leading order a particle will follow a closed orbit and not translate on average irrespective of its initial position:

$$\langle\mathbf{u}_1^L\rangle=\mathbf{0}.\tag{78}$$

We note that, while related, this statement is different from the statement that the time-averaged Eulerian velocity at a given position in the channel is zero. The time-averaged Eulerian velocity represents an average of the velocities of all particles passing through a given position in the lab reference frame, while the time-averaged Lagrangian velocity is the average velocity of a given fluid particle over time. In general, these quantities differ.[20]

Using (27) and (33), Eqs. (77) can be integrated analytically to find an exact expression for this closed orbit,

$$X_1(t)=\mathrm{Re}\left\{\iota(1-e^{-\iota t})\left[\frac{e^{\iota\kappa X_0}A(Y_0)}{\sinh(\kappa)}+\frac{B(Y_0)}{\kappa}\right]\right\}$$

$$+\alpha^{-1}X_{11}(t),\tag{79a}$$

$$Y_1(t)=\frac{(\cos(\kappa X_0-t)-\cos(\kappa X_0))\sinh(\kappa(1-Y_0))}{\sinh(\kappa)}$$

$$+\alpha^{-1}Y_{11}(t),\tag{79b}$$

where the functions giving the $O(\alpha^{-1})$ corrections,

$$X_{11}(t)=\int_0^t u_{01}(X_0,Y_0,s)ds,$$

$$Y_{11}(t)=\int_0^t v_{01}(X_0,Y_0,s)ds,\tag{80}$$

have been explicitly calculated using *Maple*, but are complicated and not given here.

To determine the nonzero ''drift'' we need to consider the Lagrangian problem at order ϵ^2,
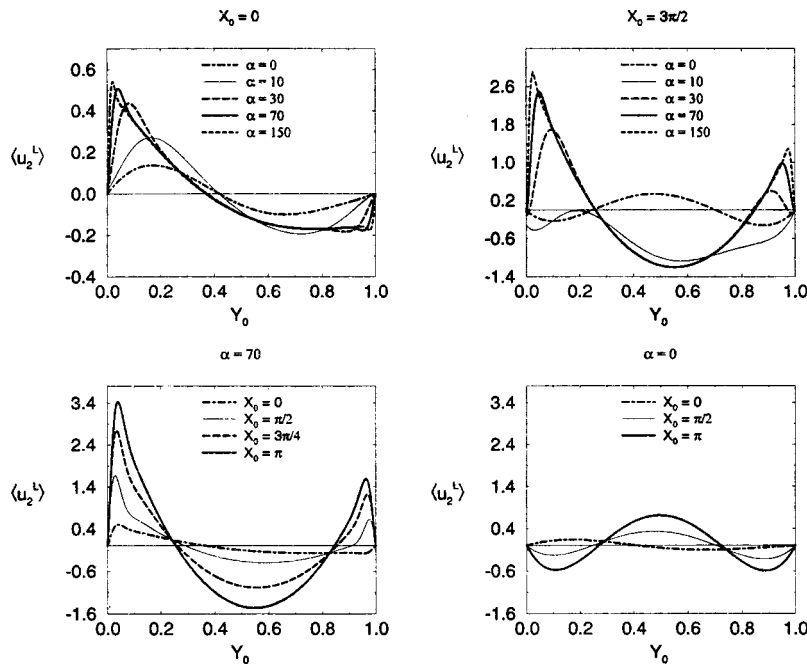
FIG. 10. The time-averaged Lagrangian velocity $\langle u_2^L \rangle$ given by (82) of a fluid particle as a function of its initial position Y_0 across the channel. The top two graphs display $\langle u_2^L \rangle$ for $\alpha = 10$ (solid thin curve), $\alpha = 30$ (long-dashed curve), $\alpha = 70$ (solid thick curve), $\alpha = 150$ (short-dashed curve) and $\alpha = 0$ (dotted–dashed curve); $X_0 = 0$ and $X_0 = 3\pi/4$; $\kappa = 1$. The $\alpha = 0$ result was computed using Eq. (71) and the analysis outlined in Sec. VI. The lower two graphs display $\langle u_2^L \rangle$ for different initial positions X_0 along the channel; $\alpha = 70$ and $\alpha = 0$.

$$u_2^L(t) = \frac{dX_2}{dt} = u_1(X_0, Y_0, t) + X_1(t)\frac{\partial u_0}{\partial x}(X_0, Y_0, t)$$

$$+ Y_1(t)\frac{\partial u_0}{\partial y}(X_0, Y_0, t), \tag{81a}$$

$$v_2^L(t) = \frac{dY_2}{dt} = v_1(X_0, Y_0, t) + X_1(t)\frac{\partial v_0}{\partial x}(X_0, Y_0, t)$$

$$+ Y_1(t)\frac{\partial v_0}{\partial y}(X_0, Y_0, t). \tag{81b}$$

Time-averaging (81), we obtain the mean Lagrangian velocity of a particle starting at $\mathbf{X}_0$,

$$\langle u_2^L \rangle = \langle u_1 \rangle(X_0, Y_0) + \left\langle X_1 \frac{\partial u_0}{\partial x}(X_0, Y_0, t) \right\rangle$$

$$+ \left\langle Y_1 \frac{\partial u_0}{\partial y}(X_0, Y_0, t) \right\rangle, \tag{82a}$$

$$\langle v_2^L \rangle = \langle v_1 \rangle(X_0, Y_0) + \left\langle X_1 \frac{\partial v_0}{\partial x}(X_0, Y_0, t) \right\rangle$$

$$+ \left\langle Y_1 \frac{\partial v_0}{\partial y}(X_0, Y_0, t) \right\rangle. \tag{82b}$$

The time averages were computed using *Maple*, but again, due to their complexity, are not presented here.

A graph of the time-averaged Lagrangian velocity $\langle u_2^L \rangle$ of a particle as a function of its initial position Y_0 across the channel is shown in Fig. 10 for $\alpha = 0, 10, 30, 70$ and 150 and $X_0 = 0$, $X_0 = 3\pi/4$. For large α (approximately $\alpha > 10$), the mean Lagrangian velocity mimics, qualitatively, the mean Eulerian velocity. Near the oscillating wall, the net flow is in the direction of the wave, while in the bulk, the flow is a return flow opposite to the wave. Near the stationary wall the Lagrangian flow can display different behavior at different

positions X_0: it may be *in the direction of the wave* (see Fig. 10 for $X_0 = 0$) or it may be *opposite* the wave direction (see Fig. 10 for $X_0 = 3\pi/4$). It can be shown that unlike the net Eulerian velocity, the net Lagrangian velocity is $O(1)$ everywhere in the channel. Figure 10 clearly shows that as $\alpha \to \infty$, the Lagrangian velocity profile, $\langle u_2^L \rangle$, converges to a universal profile similar to the curve of $\alpha = 150$.

We note that this high-frequency velocity profile differs qualitatively from the corresponding low-frequency Lagrangian transport result [see $\alpha = 0$ curve in Fig. 10 which was computed using the low-frequency asymptotic velocity profile (71) and the analysis employed in the present section], for which the net flow is *in the direction opposite to the wave* near the walls, and in the direction of the wave in the bulk for almost all X_0. The low-frequency calculation confirms the particle trajectory conclusions of Shapiro and co-workers,[18,19] Yin and Fung,[12] and Takabatake and Ayukawa.[21]

VII. CONCLUSIONS

We have calculated the time-independent streaming velocity field in a rectangular channel, whose boundary undergoes transverse traveling-wave displacements. The analysis was performed analytically for arbitrary frequencies (Appendix A), and asymptotically for the case of high frequencies ($\alpha \gg 1$), which is the relevant case for small geometries, as is the case for MEMS.[2,3] The dependence of the velocity field on α at different locations across the channel is clearly shown, which is a result that cannot be obtained simply from the exact solution for arbitrary α. The resulting flow has a boundary-layer structure, with maximum pumping occurring near the moving boundary. Near both walls the net flow is in the direction of the traveling wave. Away from the walls, there is a return flow in the opposite direction due to the fact that the channel is closed. These features are manifested both

in the Eulerian and the Lagrangian description of the flow for high frequencies, and are consistent with a laboratory scale experiment (Appendix C). At low frequencies, however, the Langrangian behavior of the flow is qualitatively different; net Langrangian transport near the walls is in the direction opposite to the wave, while in the bulk it is in the direction of the wave for most positions X_0 along the channel.

The high-frequency asymptotic solution for the Eulerian time average provides a good approximation of the exact solution even at $\alpha > 10$. For low values of α, the low-frequency asymptotic formula (71) can be used to approximate the velocity distribution. Nevertheless, particle transport is quantified by a Lagrangian calculation, which for these time-dependent flows can lead to qualitatively different results.

One application of surface-driven flows is to transport. In very small channels, such as microdevices under development, mixing will eventually occur through diffusion even without any circulation present. Mixing times across channels with characteristic length h will be $O(h^2/D)$, where $D = k_B T/6\pi\mu a$ is the Stokes–Einstein translational diffusion coefficient, where k_B is the Boltzmann constant, T is the absolute temperature and a is the radius of the diffusing molecule. To transport material along the length of the channel requires times $O((L/h)^2)$ longer. Typically, $D = 10^{-5}$ cm^2/s for most small molecules in water and can be a factor of 10–100 times smaller for large globular protein molecules. To transport (and ultimately mix) efficiently by stirring using the peristaltic motion method and device described above, it is necessary to achieve shorter transport times. Typical times for such convective transport are $O(1/\epsilon^2\omega)$, where ϵ is the dimensionless amplitude and ω is the frequency of the oscillation of the wall (see Fig. 1), since convective velocities are $O(\epsilon^2\omega h)$. This implies that wave frequencies should be $O(D/\epsilon^2 h^2)$ or larger, which is certainly reasonable in small devices.[2,3] For larger molecules, even smaller frequencies will produce convective flows that enhance transport above that from diffusion. Typical MEMS applications, for example those using piezoelectric driving, will have small surface oscillation amplitudes, $\epsilon \ll 1$, and $h = O(10^{-2}$ cm). Thus, in dimensional quantities, convective transport in aqueous solutions requires frequencies $\omega \gg 10^3$ Hz (corresponding to $\alpha \gg 1$), which is reasonable given existing demonstration devices.

ACKNOWLEDGMENTS

APPENDIX A: ANALYTICAL SOLUTION FOR ALL α

This appendix discusses the solution to Eqs. (11), (35), and (36) for arbitrary values of the dimensionless frequency parameter α. An analogous solution was first presented by Fung and Yih.[11] As described in the Introduction, the problem at hand can be solved using a perturbation expansion in ϵ. At leading order, we solve the unsteady Stokes equations,

$$\nabla^2\mathbf{u}_0 - \nabla p_0 = \alpha^2 \frac{\partial \mathbf{u}_0}{\partial t}, \quad \nabla \cdot \mathbf{u}_0 = 0, \quad (A1a)$$

$$\mathbf{u}_0(x,0,t) = (0, \sin(\kappa x - t)), \quad \mathbf{u}_0(x,1,t) = \mathbf{0}, \quad (A1b)$$

with the volume flux constraint (7). We seek a solution consisting of a part periodic in $\kappa x - t$ and a part independent of x and periodic in t.

To find the part periodic in $\kappa x - t$, introduce a stream function $\Psi_0(x,y,t)$ such that

$$\mathcal{U}_0 = -\frac{\partial \Psi_0}{\partial y}, \quad \mathcal{V}_0 = \frac{\partial \Psi_0}{\partial x}, \quad (A2)$$

which ensures that the continuity equation is satisfied. The function Ψ_0 satisfies

$$\nabla^4\Psi_0 = \alpha^2 \frac{\partial}{\partial t} \nabla^2\Psi_0. \quad (A3)$$

We seek a solution in the form

$$\Psi_0(x,y,t) = \mathrm{Re}\{\kappa^{-1} e^{\iota(\kappa x - t)} \Psi(y)\}, \quad (A4)$$

where the complex function $\Psi(y)$ is the solution to the ordinary differential equation

$$\left(\frac{d^2}{dy^2} - \kappa^2\right)\left(\frac{d^2}{dy^2} - m^2\right)\Psi = 0, \quad (A5)$$

with $m^2 = \kappa^2 - \iota\alpha^2$, and must satisfy the boundary conditions

$$\Psi(0) = 1, \quad \Psi(1) = 0, \quad \frac{d\Psi}{dy}(0) = 0, \quad \frac{d\Psi}{dy}(1) = 0. \quad (A6)$$

The solution to (A5), (A6) is

$$\Psi(y) = A \sinh(\kappa(1-y)) + B \cosh(\kappa(1-y))$$
$$+ C \sinh(m(1-y)) + D \cosh(m(1-y)), \quad (A7)$$

where

$$A = \frac{\sinh(\kappa) - \dfrac{m}{\kappa}\sinh(m)}{\left(\sinh(\kappa) - \dfrac{m}{\kappa}\sinh(m)\right)\left(\sinh(\kappa) - \dfrac{\kappa}{m}\sinh(m)\right) - (\cosh(\kappa) - \cosh(m))^2}, \quad (A8)$$

$$B = -A \frac{\cosh(\kappa) - \cosh(m)}{\sinh(\kappa) - \dfrac{m}{\kappa}\sinh(m)}, \quad C = -A \frac{\kappa}{m}, \quad D = -B.$$

Phys. Fluids, Vol. 13, No. 7, July 2001

Peristaltically driven flows for micromixers   1855

Knowing $\Psi(y)$, the leading-order velocity and pressure fields periodic in $\kappa x - t$, $\mathcal{U}_0$, $\mathcal{V}_0$, and $\mathcal{P}_0$, can be computed for any κ, α, though concise analytic expressions are difficult to write since this involves taking the real part of a complicated complex quantity.

The x-independent part of $\mathbf{u}_0$ satisfies the equations

$$\frac{\partial V_0}{\partial y} = 0, \tag{A9a}$$

$$\frac{\partial^2 U_0}{\partial y^2} - \frac{\partial P_0}{\partial x} = \alpha^2 \frac{\partial U_0}{\partial t}, \tag{A9b}$$

$$-\frac{\partial P_0}{\partial y} = \alpha^2 \frac{\partial V_0}{\partial t}, \tag{A9c}$$

subject to boundary conditions and integral constraint

$$\mathbf{U}_0(0,t) = \mathbf{0}, \quad \mathbf{U}_0(1,t) = \mathbf{0}, \quad \int_0^1 U_0(y,t)\, \mathrm{d}y = \frac{\cos(t)}{\kappa}. \tag{A10}$$

From (A9) and (A10) it is clear that $V_0 = 0$. We seek $U_0(y,t)$ and $P_0(x,t)$ of the form

$$U_0(y,t) = \mathrm{Re}\{e^{\iota t} f(y)\}, \quad P_0(x,t) = x\, \mathrm{Re}\{e^{\iota t} g\}, \tag{A11}$$

where g is a complex constant.

The unknown complex function $f(y)$ satisfies

$$\frac{\partial^2 f}{\partial y^2} - \alpha^2 \iota f = g, \tag{A12}$$

$$f(0) = 0, \quad f(1) = 0, \quad \int_0^1 f(y)\, \mathrm{d}y = \frac{1}{\kappa}. \tag{A13}$$

The solution to (A13) is easily found to be

$$f(y) = E\, \cosh(\alpha\sqrt{\iota} y) + F\, \sinh(\alpha\sqrt{\iota} y) - E, \tag{A14}$$

where

$$E = -\frac{\alpha(e^{\alpha\sqrt{2\iota}} + 1)}{\kappa(e^{\alpha\sqrt{2\iota}}(\alpha + \iota\sqrt{2} - \sqrt{2}) + \alpha - \iota\sqrt{2} + \sqrt{2})}, \tag{A15a}$$

$$F = \frac{\alpha(e^{\alpha\sqrt{2\iota}} - 1)}{\kappa(e^{\alpha\sqrt{2\iota}}(\alpha + \iota\sqrt{2} - \sqrt{2}) + \alpha - \iota\sqrt{2} + \sqrt{2})}. \tag{A15b}$$

Knowing $f(y)$, the leading-order velocity and pressure fields $U_0(y,t)$ and $P_0(x,t)$ can be computed for any κ, α, though again concise analytic expressions are lengthy to write and will not be disclosed here.

It is clear that the leading order velocity $\mathbf{u}_0(x,y,t)$ is time-periodic with zero average in time. To determine the nonzero mean flow, we consider the time-averaged first-order equations and boundary conditions,

$$\nabla^2 \langle \mathbf{u}_1 \rangle - \nabla \langle p_1 \rangle = \alpha^2 \langle \mathbf{u}_0 \cdot \nabla \mathbf{u}_0 \rangle, \quad \nabla \cdot \langle \mathbf{u}_1 \rangle = 0, \tag{A16a}$$

$$\langle \mathbf{u}_1(x,0,t) \rangle = \left\langle -\cos(\kappa x - t) \frac{\partial \mathbf{u}_0}{\partial y}(x,0,t) \right\rangle, \quad \langle \mathbf{u}_1(x,1,t) \rangle = \mathbf{0}, \tag{A16b}$$

where $\langle \cdot \rangle = (1/2\pi)\int_0^{2\pi}(\cdot)\mathrm{d}t$ denotes the time average of $(\cdot)$.

The first-order time-averaged velocity $\langle \mathbf{u}_1 \rangle$ consists of two linearly independent parts: a part independent of x, $\langle \mathbf{U}_1 \rangle(y)$, and a part periodic in x, $\langle \mathcal{U}_1 \rangle(x,y)$. The x-independent part $\langle \mathbf{U}_1 \rangle(y)$ satisfies the following equations in terms of $\Psi(y)$ computed above:

$$\nabla^2 \langle \mathbf{U}_1 \rangle - \nabla \langle P_1 \rangle = \frac{\alpha^2}{2}\left(\frac{1}{\kappa}\frac{\mathrm{d}}{\mathrm{d}y}\left(\frac{\mathrm{d}\Psi_r}{\mathrm{d}y}\Psi_i \right.\right.$$
$$\left.\left. - \Psi_r \frac{\mathrm{d}\Psi_i}{\mathrm{d}y} \right), \frac{\mathrm{d}}{\mathrm{d}y}(\Psi_r^2 + \Psi_i^2) \right), \tag{A17a}$$

$$\langle \mathbf{U}_1 \rangle(0) = \frac{1}{2\kappa}\left(\frac{\mathrm{d}^2\Psi_r}{\mathrm{d}y^2}(0), 0 \right), \tag{A17b}$$

where Ψ_r and Ψ_i are, respectively, the real and imaginary parts of Ψ. The right-hand sides of (A17) are functions of y only. Equations (A17) can thus be integrated and the solution found to be

$$\langle U_1 \rangle(y) = (1-y)\left(\frac{1}{2}\frac{\mathrm{d}P_1}{\mathrm{d}x}y + \frac{1}{2\kappa}\frac{\mathrm{d}^2\Psi_r}{\mathrm{d}y^2}(0) \right)$$
$$+ \frac{\alpha^2}{2}\int_0^y \int_0^{\bar{y}} \frac{1}{\kappa}\frac{\mathrm{d}}{\mathrm{d}y}\left(\frac{\mathrm{d}\Psi_r}{\mathrm{d}y}\Psi_i - \Psi_r \frac{\mathrm{d}\Psi_i}{\mathrm{d}y} \right)(s)\,\mathrm{d}s\,\mathrm{d}\bar{y}$$
$$- y\frac{\alpha^2}{2}\int_0^1 \int_0^{\bar{y}} \frac{1}{\kappa}\frac{\mathrm{d}}{\mathrm{d}y}\left(\frac{\mathrm{d}\Psi_r}{\mathrm{d}y}\Psi_i - \Psi_r \frac{\mathrm{d}\Psi_i}{\mathrm{d}y} \right)(s)\,\mathrm{d}s\,\mathrm{d}\bar{y}, \tag{A18a}$$

$$\langle V_1 \rangle = 0, \tag{A18b}$$

$$\langle P_1 \rangle = P_1(x) - \frac{\alpha^2}{2}|\Psi|^2, \tag{A18c}$$

where $|\Psi| = (\Psi_r^2 + \Psi_i^2)^{1/2}$ is the absolute value of Ψ.

The x-periodic part of the first-order time-averaged velocity, $\langle \mathcal{U}_1 \rangle(x,y)$, satisfies Eqs. (42) subject to the boundary conditions

$$\langle \mathcal{U}_1 \rangle(x,1) = 0, \tag{A19a}$$

$$\langle \mathcal{U}_1 \rangle(x,0) = -\frac{1}{2\pi}\int_0^{2\pi} \cos(\kappa x - t)\frac{\mathrm{d}U_0}{\mathrm{d}y}(0,t)\, \mathrm{d}t$$
$$= C_1(\kappa)\cos(\kappa x) + C_2(\kappa)\sin(\kappa x), \tag{A19b}$$

$$\langle \mathcal{V}_1 \rangle(x,0) = 0, \quad \langle \mathcal{V}_1 \rangle(x,1) = 0. \tag{A19c}$$

We use a stream function $\Psi_1(x,y)$ such that

$$\mathcal{U}_1(x,y) = -\frac{\partial \Psi_1}{\partial y}, \quad \mathcal{V}_1(x,y) = \frac{\partial \Psi_1}{\partial x}. \tag{A20}$$

The stream function $\Psi_1(x,y)$ satisfies

$$\nabla^4 \Psi_1 = -\alpha^2 \nabla \wedge \langle \mathbf{U}_0 \cdot \nabla \mathbf{u}_0 + \mathbf{u}_0 \cdot \nabla \mathbf{U}_0 \rangle, \tag{A21}$$

where the right-hand side is a function periodic in x,

$$\nabla^4 \Psi_1 = \alpha^2(f_1(y)\cos(\kappa x) + f_2(y)\sin(\kappa x)). \tag{A22}$$

We seek a solution of the form

$$\Psi_1(x,y) = \Psi_{11}(y)\cos(\kappa x) + \Psi_{12}(y)\sin(\kappa x). \tag{A23}$$

The two functions $\Psi_{11}(y)$ and $\Psi_{12}(y)$ satisfy the nonhomogeneous fourth-order ODEs,

$$\left(\frac{\partial^2}{\partial y^2}-\kappa^2\right)^2 \Psi_{11}(y)=\alpha^2 f_1(y),$$

$$\left(\frac{\partial^2}{\partial y^2}-\kappa^2\right)^2 \Psi_{12}(y)=\alpha^2 f_2(y), \tag{A24a}$$

$$\Psi_{11}(0)=0, \ \Psi_{11}(1)=0, \ \frac{d\Psi_{11}}{dy}(0)=C_1(\kappa), \ \frac{d\Psi_{11}}{dy}(1)=0, \tag{A24b}$$

$$\Psi_{12}(0)=0, \ \Psi_{12}(1)=0, \ \frac{d\Psi_{12}}{dy}(0)=C_2(\kappa), \ \frac{d\Psi_{12}}{dy}(1)=0. \tag{A24c}$$

We solve Eqs. (A24) using the symbolic manipulation package *Maple*. These allow us to compute the first-order x-periodic time-averaged velocities $\langle \mathcal{U}_1\rangle(x,y)$ and $\langle \mathcal{V}_1\rangle(x,y)$. The results cannot be disclosed here, since the expressions are long and cumbersome to write.

The first-order time-averaged velocity $\langle \mathbf{u}_1\rangle(x,y)$ is the sum of its x-independent and x-periodic parts, $\langle \mathbf{u}_1\rangle(x,y) = \langle \mathbf{U}_1\rangle(y) + \langle \mathcal{U}_1\rangle(x,y)$.

A graph of this exact solution is shown in Fig. 8, which also shows the asymptotic solution developed in the main body of the paper. For the high-frequency range $\alpha \gg 1$, the two solutions are in a good agreement.

APPENDIX B: DETAILS OF THE MATCHING PROCEDURE FOR THE $O(\alpha^{-1})$ CORRECTION TO THE LEADING-ORDER SOLUTION

Consider the velocity contribution $\mathbf{u}_0$ at leading-order in ϵ. For $\alpha \gg 1$ we confront a boundary-layer problem and consequently divide the problem into an outer and inner part. The form of the inner Eqs. (18) suggests a solution of the form,

$$\mathbf{u}_0 = \mathbf{u}_{00} + \alpha^{-1}\mathbf{u}_{01}, \tag{B1}$$

where the $\mathbf{u}_{0i}$'s are independent of α. The solution to the leading-order in α problem, $\mathbf{u}_{00}$, is outlined in the body of the paper. This appendix treats the correction $\mathbf{u}_{01}$.

Away from the walls, the correction $\mathbf{u}_{01}$ obeys the equations,

$$\frac{\partial u_{01}^o}{\partial x}+\frac{\partial v_{01}^o}{\partial y}=0, \tag{B2a}$$

$$\frac{\partial u_{01}^o}{\partial t}+\frac{\partial p_{01}'^o}{\partial x}=0, \tag{B2b}$$

$$\frac{\partial v_{01}^o}{\partial t}+\frac{\partial p_{01}'^o}{\partial y}=0, \tag{B2c}$$

where a superscipt o indicates that this is the outer solution to a boundary-layer problem. The boundary conditions cannot be stated *a priori* and need to be determined by matching the outer solution with the inner solutions. A general solution to (B2) is given by

$$u_{01}^o(x,y,t)=\cos(\kappa x-t)(E \ \cosh(\kappa y)+F \ \sinh(\kappa y))$$
$$+\sin(\kappa x-t)(G \ \cosh(\kappa y)+H \ \sinh(\kappa y))$$
$$+\frac{\sqrt{2}}{\kappa}(\cos(t)+\sin(t)), \tag{B3a}$$

$$v_{01}^o(x,y,t)=\sin(\kappa x-t)(E \ \sinh(\kappa y)+F \ \cosh(\kappa y))$$
$$-\cos(\kappa x-t)(G \ \sinh(\kappa y)+H \ \cosh(\kappa y)), \tag{B3b}$$

where the constants are to be determined by the matching. Near the walls, the correction $\mathbf{u}_{01}$ obeys the equations

$$\frac{\partial u_{00}^i}{\partial x}+\frac{\partial v_{01}^i}{\partial y'}=0, \tag{B4a}$$

$$\frac{\partial^2 u_{01}^i}{\partial y'^2}-\frac{\partial p_{01}'^i}{\partial x}=\frac{\partial u_{01}^i}{\partial t}, \tag{B4b}$$

$$\frac{\partial^2 v_{00}^i}{\partial y'^2}-\frac{\partial p_{01}'^i}{\partial y'}=\frac{\partial v_{00}^i}{\partial t}, \tag{B4c}$$

where a superscript i indicates that this is the inner solution to a boundary-layer problem. The inner solutions must satisfy homogeneous boundary conditions at their corresponding walls. That is,

$$\mathbf{u}_{01}^{i0}(x,y'=0)=\mathbf{u}_{01}^{i1}(x,y^*=1)=\mathbf{0}. \tag{B5}$$

The behavior of the inner solutions away from the walls is found by matching.

Since u_{00}^i and v_{00}^i are known, Eqs. (B4) can be solved. Near $y=0$ the general solution satisfying boundary conditions (B5) can be written in the form

$$u_{01}^{i0}(x,y',t)=\kappa \ \cos(\kappa x-t)y'-(A \ \sin(\kappa x-t)-B \ \cos(\kappa x$$
$$-t))+e^{-(\sqrt{2}/2)y'}\left(A \ \sin\left(\kappa x-t+\frac{\sqrt{2}}{2}y'\right)\right.$$
$$\left.-B \ \cos\left(\kappa x-t+\frac{\sqrt{2}}{2}y'\right)\right)$$
$$-\frac{\sqrt{2}}{\kappa}e^{-(\sqrt{2}/2)y'}\left(\cos\left(\frac{\sqrt{2}}{2}y'-t\right)\right.$$
$$\left.-\sin\left(\frac{\sqrt{2}}{2}y'-t\right)\right)+\frac{\sqrt{2}}{\kappa}(\cos(t)+\sin(t)), \tag{B6a}$$

$$v_{01}^{i0}(x,y',t)=-\kappa \ \sin(\kappa x-t)\coth(\kappa)y'+\frac{\sqrt{2}}{2}\kappa\coth(\kappa)$$
$$\times(\sin(\kappa x-t)+\cos(\kappa x-t))$$
$$-\frac{\sqrt{2}}{2}\kappa\coth(\kappa)e^{-(\sqrt{2}/2)y'}\left(\sin\left(\kappa x-t\right.\right.$$
$$\left.+\frac{\sqrt{2}}{2}y'\right)+\cos\left(\kappa x-t+\frac{\sqrt{2}}{2}y'\right)\bigg). \tag{B6b}$$

Phys. Fluids, Vol. 13, No. 7, July 2001

Peristaltically driven flows for micromixers   1857

In a similar manner, the solution near the boundary $y = 1$ is given by

$$u_{01}^{i1}(x, y^*, t)$$

$$= (C \sin(\kappa x - t) + D \cos(\kappa x - t))$$

$$- e^{-(\sqrt{2}/2)(1-y^*)} \left(C \sin\left(\kappa x - t + \frac{\sqrt{2}}{2}(1-y^*)\right) \right.$$

$$\left. + D \cos\left(\kappa x - t + \frac{\sqrt{2}}{2}(1-y^*)\right) \right)$$

$$- \frac{\sqrt{2}}{\kappa} e^{-(\sqrt{2}/2)(1-y^*)} \left(\cos\left(\frac{\sqrt{2}}{2}(1-y^*) - t\right) \right.$$

$$\left. - \sin\left(\frac{\sqrt{2}}{2}(1-y^*) - t\right) \right) + \frac{\sqrt{2}}{\kappa}(\cos(t) + \sin(t)),$$

$$(B7a)$$

$$v_{01}^{i1}(x, y^*, t)$$

$$= \kappa \operatorname{csch}(\kappa) \sin(\kappa x - t)(1 - y^*)$$

$$- \frac{\sqrt{2}}{2} \kappa \operatorname{csch}(\kappa)(\sin(\kappa x - t)$$

$$+ \cos(\kappa x - t)) + \frac{\sqrt{2}}{2} \kappa \operatorname{csch}(\kappa) e^{-(\sqrt{2}/2)(1-y^*)}$$

$$\times \left(\sin\left(\kappa x - t + \frac{\sqrt{2}}{2}(1-y^*)\right) \right.$$

$$\left. + \cos\left(\kappa x - t + \frac{\sqrt{2}}{2}(1-y^*)\right) \right).$$

$$(B7b)$$

We note that the inner representations of the velocities across the channel, v_{01}^{i0} and v_{01}^{i1}, are completely determined by the homogeneous boundary conditions at the walls, and thus do not contain any unknown constants.

To construct a representation of $\mathbf{u}_{01}$ valid uniformly throughout the channel, we must match the outer and inner representations. In doing so, we must take into account the leading-order velocity $\mathbf{u}_{00}$. Since the boundary-layer thickness scales with α, there is a coupling between $\mathbf{u}_{01}$ and $\mathbf{u}_{00}$, requiring that matching is done directly on $\mathbf{u}_0 = \mathbf{u}_{00} + \alpha^{-1} \mathbf{u}_{01}$. We rewrite the outer representation of $\mathbf{u}_0$ in terms of the inner variables y' and y^*, and require that the behavior of the outer representation $\mathbf{u}_0^o = \mathbf{u}_{00}^o + \alpha^{-1} \mathbf{u}_{01}^o$ near the walls matches asymptotically the behavior of the corresponding inner representations $\mathbf{u}_0^{i0} = \mathbf{u}_{00}^{i0} + \alpha^{-1} \mathbf{u}_{01}^{i0}$ and $\mathbf{u}_0^{i1} = \mathbf{u}_{00}^{i1} + \alpha^{-1} \mathbf{u}_{01}^{i1}$ away from the walls,

$$\lim_{\alpha \to \infty} \mathbf{u}_0^o(\alpha^{-1} y') \sim \mathbf{u}_0^{i0}(y')|_{y' \gg 1},$$

$$\lim_{\alpha \to \infty} \mathbf{u}_0^o(1 - \alpha^{-1}(1 - y^*)) \sim \mathbf{u}_0^{i1}(y^*)|_{-y^* \gg 1}. \quad (B8)$$

The constants in the above solutions can then be determined to be

$$E = -\frac{\sqrt{2}}{2} \kappa(\operatorname{csch}^2(\kappa) + \coth^2(\kappa)), \quad F = \frac{\sqrt{2}}{2} \kappa \coth(\kappa),$$

$$(B9a)$$

$$G = -E, H = -F, \quad A = E, B = E, \quad (B9b)$$

$$C = \sqrt{2} \kappa \coth(\kappa) \operatorname{csch}(\kappa), \quad D = -C. \quad (B9c)$$

The resulting outer and inner representations are given in Eqs. (33). The corresponding pressures are

$$p_{01}^{\prime o}(x, y, t) = \frac{\sqrt{2}}{2}(\cos(\kappa x - t) - \sin(\kappa x - t))$$

$$\times (\coth(\kappa) \sinh(\kappa y) - (\operatorname{csch}^2(\kappa)$$

$$+ \coth^2(\kappa)) \cosh(\kappa y)) - \frac{\sqrt{2}}{\kappa} x(\cos(t)$$

$$- \sin(t)), \quad (B10a)$$

$$p_{01}^{\prime i0}(x, y, t) = \frac{\sqrt{2}}{2} \cos(\kappa x - t) y' - \frac{\sqrt{2}}{2}(\operatorname{csch}^2(\kappa)$$

$$+ \coth^2(\kappa))(\cos(\kappa x - t) + \sin(\kappa x - t))$$

$$- \frac{\sqrt{2}}{\kappa} x(\cos(t) - \sin(t)), \quad (B10b)$$

$$p_{01}^{\prime i1}(x, y, t) = \sqrt{2} \coth(\kappa) \operatorname{csch}(\kappa)(\cos(\kappa x - t)$$

$$- \sin(\kappa x - t)) - \frac{\sqrt{2}}{\kappa} x(\cos(t) - \sin(t)).$$

$$(B10c)$$

APPENDIX C: EXPERIMENTAL DEMONSTRATION OF PERISTALTIC TRANSPORT AT HIGH (DIMENSIONLESS) FREQUENCIES

1. Description of the apparatus

An apparatus was designed and constructed to model microscale flow in a MEMS mixing device, such as described in the main body of the paper. Qualitative results from the experiments using small amplitude traveling waves indicate good agreement with the theory developed. As expected, there are qualitative differences with the (large amplitude) results of the experiments of Yin and Fung[12] which are performed at low pumping frequencies and therefore expected to exhibit opposite reflux behavior.

The mixing chamber measured 10 cm square, with a height $h = 1$ cm, and was made of acrylic except for the lower boundary which consisted of a thin (0.02 cm thickness) latex sheet, as illustrated in Fig. 11. Fluid motion was driven by a traveling wave generated on the flexible latex boundary by the teeth of a timing belt, which created in the latex sheet depressions approximating a sine wave. The belt was mounted on pulleys driven by an adjustable speed motor, so that a range of traveling wave frequencies could be obtained. The oscillatory motion in the latex sheet was easily observable, and found to be regular by using a strobe light. The wavelength of the traveling wave was determined by the
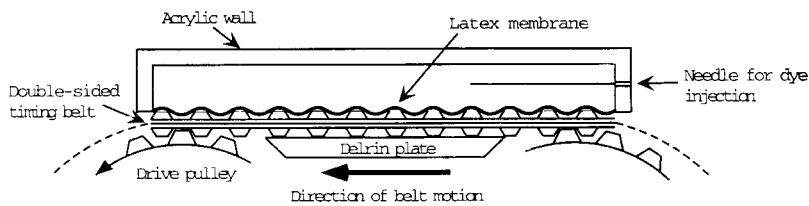
FIG. 11. Schematic diagram of the experimental apparatus.

pitch of the timing belt, which here was 0.508 cm. The working fluid was an 80 wt % mixture of glycerol and water.

In the experiments reported here, the wave had a dimensionless amplitude $\epsilon = b/h \approx 0.01$ and the frequency was $\omega \approx 90$ rad/s (about 15 timing belt teeth passing by per second), which corresponds to a dimensionless wave number $\kappa = kh \approx 12$, and dimensionless frequency $\alpha^2 = \omega h^2/\nu \approx 200$. These values correspond to the case considered analytically in Secs. III–IV for large α, and present a reasonable laboratory scale model of a MEMS device in which wave amplitudes are small. This motion, however, is unlike typical peristaltic pumping in biological systems where wave amplitudes are large and the channel walls actually come into (near) contact.

Flow visualization was achieved by injecting dye into the mixing chamber with a 20-gauge needle through a rubber septum mounted on the side wall (which allowed a range of motions for the needle). The injection point was near the center of the box, so that side-wall effects were minimized. Laser light sheet illumination of neutrally buoyant hollow glass spheres was also used for flow visualization. The motion of the glass particles indicated the velocity of the fluid at each point in the chamber. The results from dye injection were most easily visible, and will be discussed here, whereas the particle tracking method potentially provides more quantitative information about the velocity throughout the mixing chamber.

2. Results and discussion

Figure 12 shows the deformation of a vertical streak of dye injected into the middle of the mixing chamber. The velocity profile obtained in the lower half of the chamber matches at least qualitatively that predicted in Fig. 8.

Near the lower boundary, it can be seen that there exists a narrow boundary layer where the velocity is in the direction of the wave motion, i.e., to the left. This is the streaming velocity with order of magnitude $O(\epsilon\omega b)$. Above this narrow boundary layer, the flow is towards the right, so there is no net flow over any cross section of the box. The velocity satisfies the no-slip condition at the sides of the box, and

therefore goes to zero at the upper boundary. This results in a pressure-driven Poiseuille flow profile in the upper region of the box. We note that a brief examination of the dye profile near the upper boundary did not reveal evidence of a boundary layer with forward flow to the left, as predicted by the analytical results in Sec. III. The velocity near the lower boundary can be estimated from Fig. 12 and compared with order of magnitude estimates obtained from the analytical model. Measurements from the figures indicate a streaming velocity u_c approximately 10^{-4} m/s. This value is in very good agreement with the velocity estimated using $u_c \approx \epsilon\omega b \approx 9 \times 10^{-5}$ m/s for the parameters in this experiment.

The experiment could be run continuously, and circulation was observed in the closed chamber by placing dye at the bottom of the chamber and following its path. The dye streak created did not diffuse very much in the glycerol-water solution and was still visible when it completed a loop in the chamber. It took approximately 5 min for the dye to traverse the length of the box along the bottom. We note that $\epsilon = 0.01$ gives a time of about 13 min to traverse 7 cm (from the injection point) along the bottom of the box, while $\epsilon = 0.015$ gives approximately 5 min. The time for the dye to travel along the upper surface to the right was much longer than the time it took to travel along the bottom, as the velocity in the lower boundary layer was much faster than elsewhere in the box. After approximately 50 min, the dye had completed a loop around the whole chamber.

The flow profiles observed agree qualitatively with those predicted by the analysis in the above paper. As discussed previously, they are quite different from those obtained by Yin and Fung[12] in a similar experiment, performed, however, in a different parameter space. In the present case, the boundary-layer region was confined to a very narrow region near the moving boundary, and only in this region were there large velocities observed. Above this boundary layer, a reverse pressure-driven Poiseuille flow was observed, where velocities were much smaller. Yin and Fung studied flow induced by a low-frequency traveling surface wave in a long channel with different applied pressure gradients, and also
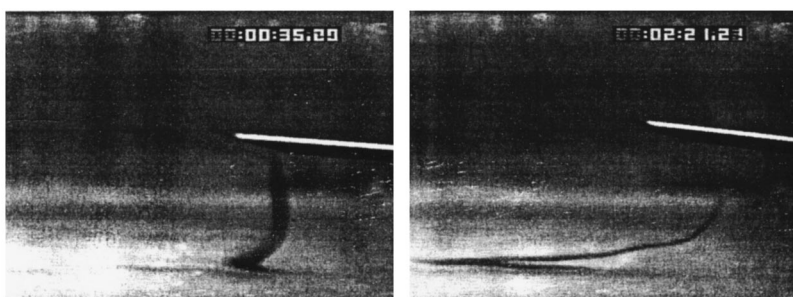

FIG. 12. Deformation of a vertical streak of dye injected from the needle tip. Fluid at the bottom of the picture moves rapidly to the left, in the direction of the traveling wave, while a slow flow to the right exists above this narrow boundary layer. The clock shows the time elapsed.

calculated particle paths in the fluid. We can compare our results to the case of zero flux flow considered by Yin and Fung, which essentially approximated a closed channel or mixing chamber. In their experiment, the parameters used were (in our notation): $\epsilon = 0.1$, $\kappa = 0.57$, $\omega = 0.314$ rad/s, and $\alpha^2 = 0.684$ (note that h denotes the channel half-height in Yin and Fung's paper). Results using these parameters are shown in Fig. 7 of their paper. The profiles observed experimentally by Yin and Fung are different from those in our experiment, in that they observed reverse flow (opposite the direction of the traveling wave) near both the upper and lower boundaries, and forward flow (in the direction of the traveling wave) only in the middle of the channel. This behavior is expected at low pumping frequencies as described in the body of our paper.

3. Conclusion

The experimental results presented show good qualitative agreement with the flow profiles predicted analytically in the main body of the paper. The parameters chosen here closely approximate the high-frequency, low-amplitude conditions characteristic of peristaltically driven MEMS designs. It was observed that circulation was possible for low amplitude driving. Though inefficient for mixing on a large scale, this experimental set-up demonstrated the capabilities of peristaltic mixing on the laboratory scale. At smaller scales such as in MEMS, the availability of high-frequency driving means that the mixing velocities should be significantly higher [due to scaling as $O(\epsilon \omega b)$] and mixing should be more efficient.

[1] *Microelectromechanical Systems (MEMS)—1998*, edited by L. Lin, F. K. Forster, N. R. Aluru, and X. Zhang (ASME, New York, 1998), DSC-Vol. 66.

[2] S. Miyazaki, T. Kawai, and M. Araragi, ''A piezoelectric pump driven by a flexural progressive wave,'' *Proceedings of the IEEE Micro Electro Mechanical Systems* (IEEE, New York, 1991), 283–288.

[3] R. M. Moroney, R. M. White, and R. T. Howe, ''Ultrasonically induced microtransport,'' *IEEE Transactions* (IEEE, New York, 1991).

[4] J. Evans, D. Liepmann, and A. P. Pisano, ''Planar laminar mixer,'' in *Proceedings IEEE. The Tenth Annual International Workshop on Micro Electro Mechanical Systems* (IEEE, New York, 1997), pp. 96–101.

[5] A. H. Shapiro, M. Y. Jaffrin, and S. L. Weinberg, ''Peristaltic pumping with long wavelengths at low Reynolds numbers,'' J. Fluid Mech. **37**, 799 (1969).

[6] K. P. Selverov and H. A. Stone, ''Peristaltically driven flows for micromixers,'' in Ref. 1, p. 85.

[7] M. Hanin, ''The flow through a channel due to transversely oscillating walls,'' Isr. J. Technol. **6**, 67 (1968).

[8] T. F. Zien and S. Ostrach, ''A long wave approximation to peristaltic motion,'' J. Fluid Mech. **3**, 63 (1970).

[9] C. Barton and S. Raynor, ''Peristaltic flow in tubes,'' Bull. Math. Biophys. **30**, 663 (1968).

[10] J. C. Burns and T. Parkes, ''Peristaltic motion,'' J. Fluid Mech. **29**, 731 (1967).

[11] T. C. Fung and C. S. Yih, ''Peristaltic transport,'' Trans. ASME, J. Appl. Mech. **35**, 669 (1968).

[12] F. C. P. Yin and Y. C. Fung, ''Comparison of theory and experiment in peristaltic transport,'' J. Fluid Mech. **47**, 93 (1971).

[13] N. Riley, ''Acoustic streaming,'' in *Encyclopedia of Acoustics*, edited by M. J. Crocker (Wiley, New York, 1997), pp. 321–327.

[14] N. Riley, ''Oscillatory viscous flows. Review and extension,'' J. Inst. Math. Appl. **3**, 119 (1967).

[15] W. L. M. Nyborg, ''Acoustic streaming,'' in *Physical Acoustics IIB*, edited by W. Mason (Academic, New York, 1965).

[16] M. S. Longuet-Higgins, ''Mass transport in water waves,'' Philos. Trans. R. Soc. London **345**, 535 (1953).

[17] C. C. Mei, *Applied Dynamics of Ocean Surface Waves* (Wiley, New York, 1983).

[18] S. L. Weinberg, E. C. Eckstein, and A. H. Shapiro, ''An experimental study of peristaltic pumping,'' J. Fluid Mech. **49**, 461 (1971).

[19] M. Y. Jaffrin and A. H. Shapiro, ''Peristaltic pumping,'' Annu. Rev. Fluid Mech. **3**, 13 (1971).

[20] A. H. Shapiro and M. Y. Jaffrin, ''Reflux in peristaltic pumping: is it determined by the Eulerian or Lagrangian mean velocity?'' Trans. ASME **38**, 1060 (1971).

[21] S. Takabatake and K. Ayukawa, ''Numerical study of two-dimensional peristaltic flows,'' J. Fluid Mech. **122**, 439 (1982).

[22] M. Yi, H. Bau, and H. Hu, ''Peristaltically induced motion in a closed cavity with two vibrating walls,'' Phys. Fluids (to be published).

[23] L. G. Leal, *Laminar Flow and Convective Transport Processes: Scaling Principles and Asymptotic Analysis* (Butterworth–Heinemann, London, 1992).

[24] M. Van Dyke, *Perturbation Methods in Fluid Mechanics* (Parabolic, Stanford, 1975).